Frictional weakening in the highly mobile 2025 Blatten (Switzerland) rock–ice avalanche

EarthArXiv Preprint Coversheet

Frictional weakening in the highly mobile 2025 Blatten (Switzerland) rock–ice avalanche

Jiahui Kang[1,2*], Antoine Lucas[3], Anne Mangeney[3, 4], Johan Gaume[5,6], Kate Allstadt[7], Clément Hibert[8,9], Liam Toney[7], Hervé Vicari[5,6], Michael Dietze[9], Mylène Jacquemart[12,13], Marc Peruzzetto[11,3], Lars Blatny[6, 14], Michael L. Kyburz[5,6], Joachim Rimpot[8], Daniel Farinotti[12,13], Fabian Walter[1*]

[1*]Swiss Federal Institute for Forest, Snow and Landscape Research WSL, Birmensdorf, Switzerland.

[2*]Faculty of Geosciences and Environment, University of Lausanne, Lausanne, Switzerland.

[3]Institut de physique du globe de Paris, Université Paris Cité, CNRS, Paris, France.

[4]Institut Universitaire de France, Paris, France.

[5] WSL Institute for Snow and Avalanche Research SLF, Davos, Switzerland.

[6] Institute for Geotechnical Engineering, ETH Zürich, Zürich, Switzerland.

[7] U.S. Geological Survey, Geologic Hazards Science Center, Golden, Colorado, USA.

[8] Institut Terre et Environnement de Strasbourg (ITES), Université de Strasbourg, Strasbourg, France.

[9] Ecole et Observatoire des Sciences de la Terre (EOST), Université de Strasbourg, Strasbourg, France.

[10] Department of Geography, RWTH Aachen University, Aachen, Germany.

[11]BRGM, F-75012, Paris, France.

[12]Laboratory of Hydraulics, Hydrology and Glaciology (VAW), ETH Zürich, Zürich, Switzerland.

[13]Swiss Federal Institute for Forest, Snow and Landscape Research WSL, Sion, Switzerland.

[14]CNRS - UMR 7190, Institut Jean Le Rond d'Alembert, Sorbonne Université, Paris, France.

*Corresponding author(s). E-mail(s): jiahui.kang@wsl.ch; fabian.walter@wsl.ch;

Abstract

Cascading slope failures in alpine environments are intensifying as glaciers retreat and slope stability adjusts to a warming climate. Yet, the mechanisms governing such large, rapidly evolving events remain poorly understood. The 28 May 2025 rock–ice avalanche from Birch Glacier, Switzerland ($\approx \mathbf{9.3 \times 10^6\ m^3}$), which devastated part of the village of Blatten, provides a rare, well-documented case to analyze the full sequence of instability and collapse. We combine state-of-the-art seismic, geomorphological, and geotechnical evidence with numerical modeling to reconstruct the evolution of the avalanche. We show that more than two weeks of accelerating rockfall activity and minor glacier collapses preceded the main detachment. The main collapse happened in four kinematic stages, from initial detachment to deposition. Only with drastically reduced friction can both depth-averaged and three-dimensional flow models reproduce the center-of-mass force history and the deposit geometry. Multiple mechanisms could have contributed to this frictional weakening such as ice content and meltwater. In-situ measurements of fine grain size and low permeability indicate possible elevated pore pressures, which would have facilitated the mobility. This work leverages multi-disciplinary datasets to investigate failure precursors and frictional regimes of catastrophic mass movements in changing climatic and permafrost conditions.

Keywords: Rock–ice avalanche, Granular flow dynamics, Seismic signatures, Geotechnical measurements, Frictional weakening

Plain Language Summary

On 28 May 2025, a rapid avalanche consisting of ice and rock buried many houses and killed one person in Switzerland's village of Blatten. This catastrophic event was preceded by two weeks of increasing rockfall activity onto a glacier, which under the added weight suddenly slipped away and produced the devastating rock-ice avalanche. As one of the best-observed events of its kind, the Blatten avalanche offers a unique opportunity to investigate both the early warning signs of rockfalls and small avalanches, as well as the main collapse. Continuous records of ground unrest from nearby seismometers document not only the rockfalls during the two weeks of growing instability but also capture details of how the main avalanche plummeted towards the valley. Using the shape, extent and material properties of the rock-ice deposits, we built numerical models to estimate (i) how much material collapsed during early instability, (ii) where the material came from (and how different source areas contributed), and (iii) how

the main failure moved and spread during the event. Taken together, this approach provides a method for hazard assessment and highlights the importance of different observations to predict runout of catastrophic mass movements in the rapidly changing Alpine environment.

Introduction

Cascading mass movements in high mountains are a rapidly growing hazard in a warming climate [1–4]. Cryosphere degradation (glacier retreat, permafrost thaw) and the intensification of hydrometeorological triggers (extreme rainfall, rapid snowmelt) are increasing the frequency and magnitude of these events, creating unprecedented risks for downstream communities [5–8]. From the Himalayas to the European Alps to the Andes, mountains are subject to a new regime of complex, cascading disasters, demanding a reassessment of the physical processes governing slope failure and runout [9–11].

Progress in understanding such events has advanced on two parallel but often disconnected fronts: pre-failure monitoring for early warning [12–15] and post-event modelling for process understanding and hazard assessment [16, 17]. However, quantitative estimates of how the released volume of small precursory events evolves before large mass failure remain elusive. In the meanwhile, numerical models are usually validated only through back-analysis of final deposits [18–20]. This reliance on end-state geometries may fail to capture the dynamics and evolving frictional regimes at play [21].

Seismic observations offer the unique potential to bridge this observational gap. They provide continuous, real-time records of slope activity and capture the forces that moving masses exert on the Earth's surface [2, 22–26]. Comparing these forces with those simulated by granular mass-movement models constrains key event properties such as volume, friction coefficient, and basal conditions [21, 27]. For instance, glacier ice within or underneath the moving mass substantially reduces basal friction to enhance mobility [16, 21, 28]. Different seismic approaches are sensitive to different parts of the failure process. Low-frequency seismic signals are typically applicable only to large events via seismic-force inversion [21, 27], whereas smaller precursor failures can instead be characterized using high-frequency seismic analyses that provide information on event volume and friction coefficient [e.g., 25, 29, 30]. Despite these advances, studies have rarely integrated pre-failure monitoring, seismic-force inversion of the main event, and independent geotechnical or geomorphological constraints within a single framework to analyze the full sequence from precursory activity to catastrophic collapse. Bridging these disciplines could move beyond empirical runout estimates and toward a transferable, mechanistic framework for predicting future cascading disasters.

On 28 May 2025, a rock–ice avalanche with an estimated volume of $9.3 \times 10^6 \mathrm{m}^3$ [31] occurred at Birch Glacier (German: Birchgletscher; Fig.1a) in Switzerland. The glacier failed under the weight of a rock cover, which had been deposited on its surface after several days of rockfalls from Kleines Nesthorn, located around 600 m above the

glacier. The rock-ice avalanche destroyed parts of the village of Blatten and resulted in one fatality.

Here, we combine high and low-frequency seismic records, geomorphological constraints, geotechnical data, and granular flow modeling to: (i) track the evolution of failure from the precursory seismic instability (quantifying precursory event volumes and inferring the friction coefficients) to the kinematic evolution of the main collapse (seismic-force inversion), (ii) quantitatively calibrate large-scale rock-ice avalanche modeling by optimizing against both seismic-force inversion and high-resolution deposit metrics, and (iii) constrain the frictional mechanisms with in-situ geotechnical measurements. We show that drastically reduced friction coefficients are needed to reproduce the observation. This frictional weakening may reflect several interacting mechanisms, including small rock-ice friction, meltwater generation, and dynamic fragmentation. Supported by geotechnical measurements, we discuss how the presence of meltwater and fine particles could have facilitated and sustained elevated pore-fluid pressures, collectively transforming rock-ice avalanches into highly mobile, catastrophic flows. Together, these results establish a multidisciplinary, data-constrained framework for predictive understanding of landslide high mobility.

Event records and characteristics

A destabilization sequence lasting more than two weeks preceded the main collapse. Rockfalls from the Kleines Nesthorn onto Birch Glacier intensified on 14 May as reported by the local authority (Fig. 1a). Because these early events were continuously recorded with regional seismic stations, they form a unique, high-resolution dataset for precursory sequence analysis. The increased rockfall activity prompted authorities to evacuate the 300 residents of Blatten as a precaution. The deposition of debris subsequently destabilized the Birch Glacier, leading to accelerated ice flow with velocities of tens of meters per day. On 27 May, an ice avalanche involving several thousands of cubic meters, according to the Lötschental Regional Command Staff [32], detached from the glacier terminus, coming to rest roughly 400 m above the Lonza River flowing along the Lötschental valley bottom (Fig. 1a).

The main collapse on 28 May mobilized $\approx 9.3 \times 10^6$ m^3 of material including $\approx 3.0 \times 10^6$ m^3 of ice [31], leaving a head scarp on the Kleines Nesthorn and an adjacent glacier-collapse scarp (Figs. 1b,f). The avalanche mobilized a maximum detachment thickness of 130 m at Kleines Nesthorn and 51 m at the glacier (Figs. 1c-e). Upon detachment, the rock-ice mass descended a narrow gorge (Fig. 1h), traversed the valley bottom and ran more than 200 m up the Weissenried counterslope (Fig. 1g). The final deposits on the valley floor were up to 34 m thick (Figs. 1d, g). The deposit dammed the Lonza River, forming a lake that flooded parts of the village.

The avalanche-generated ground motion was equivalent to an M_L 3.1 earthquake, where M_L is the local magnitude [33]. It generated strong long-period (15–180 s) surface waves that were recorded at distances exceeding hundreds of kilometers (Fig. 1j). Station LAUCH (Fig. 1a) (≈ 5 km away) recorded a signal of around 100 s duration, with an emergent onset and peak ground velocities exceeding 10^{-4} m/s (Fig. 1i).

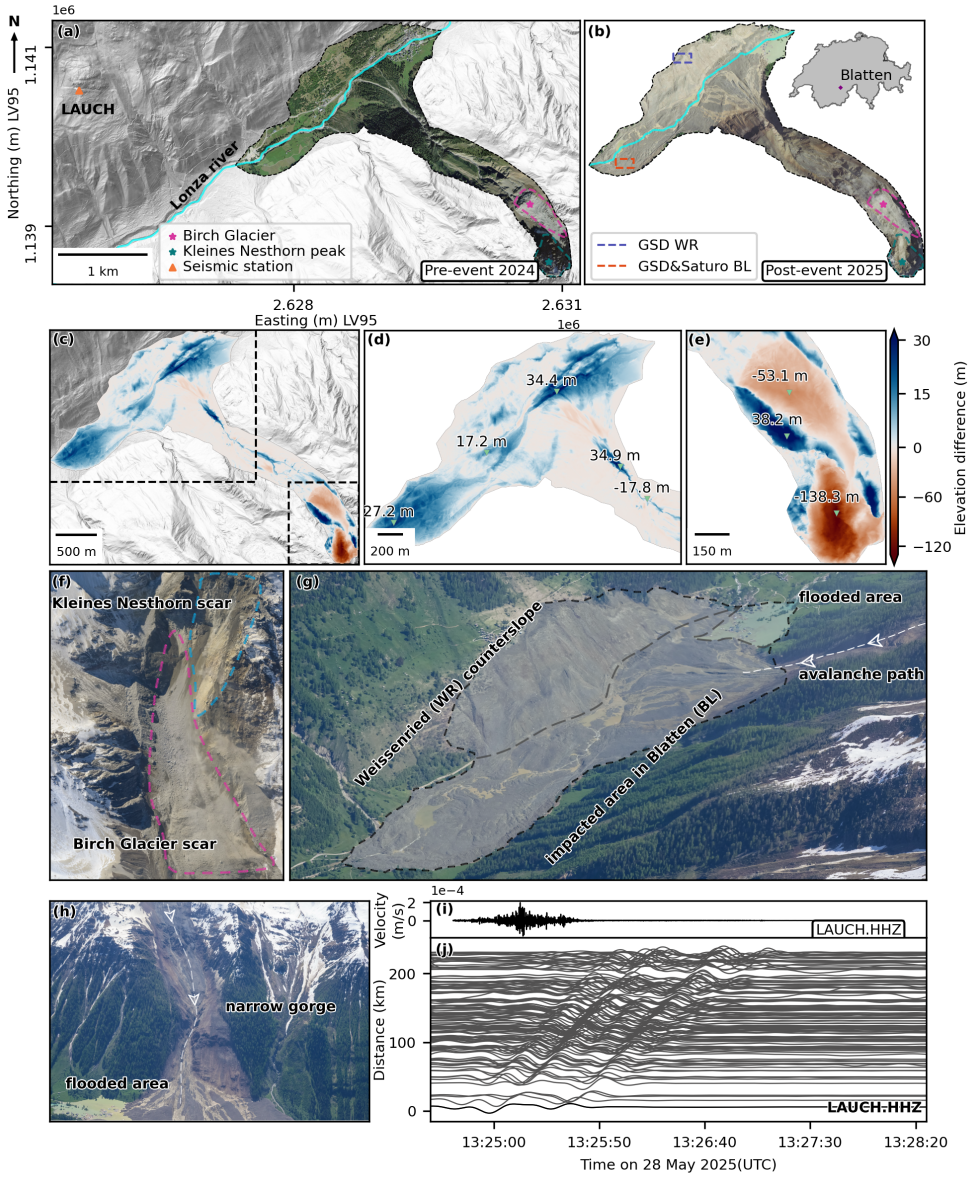

Fig. 1: Overview of the Blatten rock-ice avalanche. (a, b) Pre-event (2024) aerial view (SWISSIMAGE 10 cm, 2024, https://www.swisstopo.admin.ch/en/orthoimage-swissimage-10) and post-event (30 May, 2025) aerial view (https://rapidmapping.admin.ch/files/en/pastevents.html). LV95 refers to the official Swiss coordinate reference system (EPSG:2056). Kleines Nesthorn, Birch Glacier, seismic station LAUCH (≈5 km away from Birch Glacier), and the Lonza River flowing along the Lötschental valley are indicated. Sampling sites of grain-size distribution (GSD) and SATURO saturated hydraulic conductivity are indicated in (b) and described in the Methods section. (c-e) Elevation differencing derived from pre- (swissALTI3D, 2024, https://www.swisstopo.admin.ch/en/height-model-swissalti3d) and post-event (29 May 2025) digital elevation models (ETH Zurich product, will be made available upon publication). (f–h) Field photographs (https://rapidmapping.admin.ch/files/en/pastevents.html). The photos show the Birch Glacier scar and Kleines Nesthorn scar, the avalanche path with a narrow gorge, the deposition area, and the area flooded by the dammed Lonza River. (i) The vertical-component (HHZ) seismic waveform recorded at LAUCH. (j) Low-frequency (15–180 s) vertical components of seismic signals of the event recorded within 300 km ordered by distance.

Precursory Destabilization Sequence

We used a self-supervised clustering algorithm [34] to quantify the precursory seismic sequence and constrain the nature of the events using continuous vertical-component data from station LAUCH (Fig. 1a) between 1 January and 1 June 2025, segmented into 40,574 180 s time windows. The method identified 236 clusters, 17 of which showed a clear increase in event counts (≈700 events, refer to Methods). These form two families based on their temporal evolution. Family 1 follows an S-shaped temporal pattern, with activity increasing after 19 May, peaking on 22 May, and then plateauing (e.g., Figs. 2e, g and Extended Data Figs. 1). Family 2 exhibits a gradual increase of event rate from 19 to 28 May (e.g., Figs. 2f, h and Extended Data Figs. 2). Whereas event frequency tracks the progression of instability, the total mobilized mass can evolve independently because the volume of individual events varies [35]. Furthermore, distinguishing the source locations is essential in this complex setting, as failures could originate from either the Kleines Nesthorn or the Birch Glacier.

We used a method [29, 30, 36] to quantify both the volume and characteristic friction of an event series based on the high-frequency seismic signals coupled with numerical simulations. This is because these small events do not produce low-frequency waves that can be reliably resolved at distant stations. This approach assumes that the scaling relation between radiated seismic energy (E_s) and signal duration (t_s) follows a power law, $E_s = \alpha t_s^{\beta}$. The exponent β serves as a proxy for flow mobility, where higher values indicate stronger energy dissipation and lower mobility (refer to Methods). Calculating this relation reveals different behaviors for the observed events: Family 1 shows $\beta = 2.38 \pm 0.18$, whereas Family 2 gives a lower $\beta = 1.80 \pm 0.15$ (Figs. 2c, d).

An equivalent power-law relation, $E_p = \alpha' t_p^{\beta'}$, links the loss of potential energy (E_p) to flow duration as shown for lab- and field-scale granular flows [29, 36]. To recover these power laws, we performed a series of simulations using the SHALlow water depth-averaged numerical model (SHALTOP) [37, 38], which solves the shallow-flow conservation equations for dense granular flows over complex terrain [17, 22, 37–42]. To distinguish source locations, we defined two possible source areas: Kleines Nesthorn (Fig. 2a) and the Birch Glacier terminus (Fig. 2b). We simulated 55 events (500-300,000 m^3) at Kleines Nesthorn and 35 events (500-30,000 m^3) at the Birch Glacier terminus, as smaller volumes were reported for the glacier failures.

Assuming that the seismic duration equals the flow duration for each event, we calibrate an energy-conversion ratio $R_{ps} = \frac{E_p}{E_s}$ by matching the duration-energy scaling exponents (β) between observations ($E_s - t_s$) and SHALTOP simulations ($E_p - t_p$). The β values are then derived from simulations using a constant Coulomb friction rheology with friction angles $\delta \in [10°, 20°, 30°]$ over a range of event volumes and for two source locations. For Kleines Nesthorn, the β values are 2.07 ± 0.24, 2.33 ± 0.20, and 3.01 ± 0.27 (Fig. 2c). For Birch Glacier terminus, they are 1.78 ± 0.15, 2.10 ± 0.19, and 2.46 ± 0.21 (Fig. 2d). Matching the seismic and simulated power laws requires the Kleines Nesthorn source and a friction angle $\delta = 20°$ for Family 1. These events are thus most probably rockfalls. In these simulations, the flow typically comes to rest and deposits on the glacier. Family 2 requires a friction angle of $\delta = 10°$ and events originating from the glacier terminus, thus corresponding to small rock–ice avalanches.

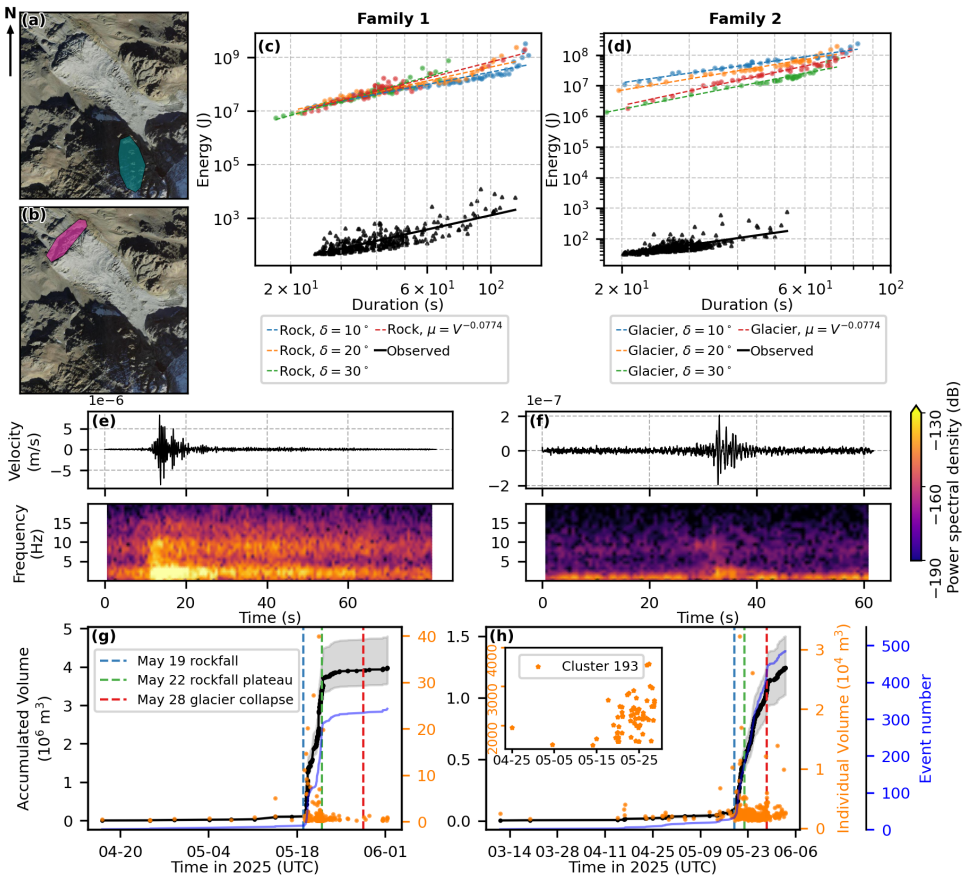

Fig. 2: Seismic analysis of the precursory destabilization sequence. The right orthophotos (SWISSIMAGE 10 cm, 2024) (a, b) show the locations of rockfall (teal) and glacier (pink) sources. (c, d) Energy-duration scaling relations used to infer relative mobility for (c) Family 1 (rockfalls depositing on the glacier) and (d) Family 2 (small rock–ice avalanches). Observed seismic events (black triangles) are directly compared to granular flow simulations (colored dashed lines and scatter points). Each color corresponds to a distinct friction angle and each point represents one simulation at a specific volume. (e, f) Representative seismic waveforms and spectrograms for Family 1 and Family 2, respectively. (g, h) Temporal evolution of the accumulated volume and event number of Family 1 and Family 2. The gray shaded envelopes represent the propagated uncertainty bounds for the volume estimate. Inset of (h) highlights cluster 193 with the y-axis being the individual volume, showing a clear trend of increasing individual event volume preceding the main collapse.

We compared the constant friction results against the empirical volume-dependent law $\mu(V) = \tan\delta = V^{-0.0774}$, which is calibrated for standard dry granular mass movements [41]. For Family 1, our best-fit constant friction $\delta = 20°$ matches the $\mu(V)$ equivalent friction angle only at the maximum simulated volume of $V = 300,000$ m^3 ($\arctan(300,000^{-0.0774}) \approx 20.6°$). This implies that the smaller precursors were more mobile than expected for typical dry granular flows, likely due to pre-existing moisture in the release mass and/or the presence of rainwater as over $\approx$ 70 mm of rainfall accumulated in May (before 28 May) [43]. Furthermore, for this family, the simulated β exponent predicted by using the $\mu(V)$ law in the simulations across the 500-300,000 m^3 volume range (2.73 ± 0.25) overestimates the observed β (2.38 ± 0.18), which confirms that these events are not dry [30]. For Family 2, the observed β (1.80 ± 0.15) is also substantially smaller than the $\mu(V)$ prediction for its 500-30,000 m^3 volume range (2.71 ± 0.20), requiring a much lower friction angle of 10° as found with the constant Coulomb friction simulations. Recent numerical simulations by Zhou et al. [44] demonstrate that adding 70% ice to a granular mixture can reduce its friction angle by half compared to pure rock. Therefore, these Family 2 events are likely small rock-ice avalanches comprised of glacier ice and deposited debris from the slope.

We estimated the individual release volumes by linking its radiated seismic energy to the physical loss of potential energy (refer to Methods). By accounting for variations in source mass density and energy conversion ratios, we established confidence envelopes for these volume estimates (refer to Methods). The cumulative seismic release for Family 1 leads to a cumulative volume reaching 3.91×10^6 m^3 (uncertainty range: 3.51×10^6 to 4.72×10^6 m^3) by 28 May. The S-shaped growth curve indicates rapid mass wasting from the Kleines Nesthorn of 3.75×10^6 m^3 (uncertainty range: 3.37×10^6 to 4.52×10^6 m^3) released by 23 May (Fig. 2g), aligning closely with the 3.50×10^6 m^3 mass loss estimated from digital elevation models (DEM) differencing. The cumulative volume of Family 2 grew steadily, reaching 1.10×10^6 m^3 (uncertainty range: 0.91×10^6 to 1.33×10^6 m^3) by 28 May. Within Family 2, Cluster 193 highlights this trend with increasing individual event volumes preceding the final collapse (Fig. 2h, inset). However, other clusters lack this clear escalation in individual event size, indicating that their cumulative mass wasting volume was primarily driven by event frequency.

Seismic inversion

To resolve the dynamics of the main rock-ice avalanche, we inverted low-frequency (15–180 s) seismic waveforms (Fig 3a) recorded at distances between 33 and 110 km. We used the *lsforce* code [45, 46] to estimate the three-dimensional (3D), time-varying equivalent single force exerted on the Earth's surface by the avalanche (Fig 3c). At long periods, this force is equal to but opposite in direction to the product of the acceleration of the center of mass of the landslide and its total mass [23, 24, 47].

We interpret four phases in the force history (Figs. 3b–e). During Phase 1 (0–51 s) the mass accelerates as the force magnitude grows steadily, reaching 6×10^{10} N. The force is directed southeast as shown at instant I (t=24 s, Figs 3b, e), opposite, as expected, to the initial acceleration of the mass. Minimal high-frequency (>1 Hz)

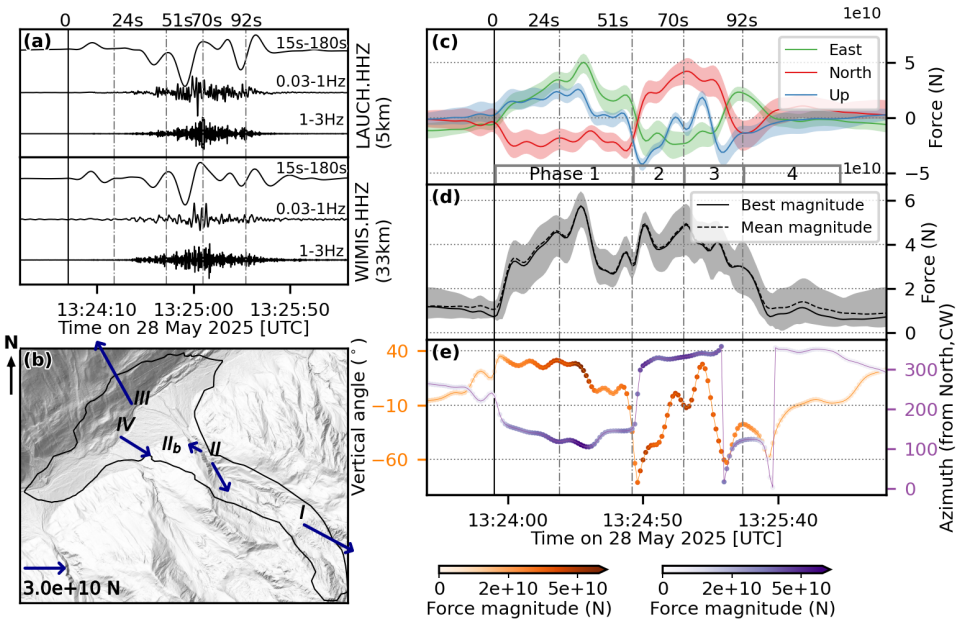

Fig. 3: Seismic force history of the 28 May 2025 main collapse. (a) Seismic waveforms from two close broadband stations, LAUCH (≈5 km) and WIMIS (≈33 km), shown in three frequency bands. Roman numerals denote four key kinematic instances discussed in the main text. (b) Shaded relief map (swissALTI3D, 2024) of the avalanche path. The approximately inferred location of the avalanche is shown for each instant with blue arrows indicating the direction and magnitude of the force. (c) Three-component inverted force history. The shaded areas represent the uncertainty range estimated using a jackknife resampling scheme. (d) Amplitude of the total inverted force vector. (e) Vertical angle and azimuth of the inverted force vector. The scattered points are color-coded with force magnitude. As the avalanche decelerates and force magnitudes approach zero towards the end of the timeframe, the markers become nearly transparent.

energy detected at LAUCH at 5 km distance during this phase indicates limited mass fragmentation [2, 19, 48, 49]. During Phase 2 (51–70 s), the mass transits the gorge and collides with the valley floor. At ≈51 s, the force azimuth abruptly rotates by ≈ 180° as the flow enters the narrow gorge. This reversal marks the transition from acceleration ($0 - II$) to deceleration (II_b, 54 s) and captures the strong centripetal forces during flow confinement. The first burst of high-frequency energy (>0.3 Hz) appears at this instant (Fig. 3a), indicating internal collisions of the rock-ice mass. As the avalanche exits the gorge and collides with the Weissenried counterslope (III, 70 s), the force reaches 5×10^{10} N and the flow radiates elevated high-frequency seismic energy. Phase 3 (70–92 s) consists of flow redirection and secondary runup. Following the impact of the avalanche with the Weissenried counterslope, the force vector swings

southwest during the backflow of material toward Blatten and the lateral spreading of the mass. A secondary force peak near 92 s corresponds to a smaller runup towards the valley side of initial descent and southwestward azimuth change, consistent with observed deposit geometry and high-frequency bursts [25]. Phase 4 (> 92 s) describes the spreading and final mass deposition. The force magnitude decays as the bulk of the rock-ice avalanche comes to rest. High-frequency radiation ceases, indicating that energetic collisions have ended and motion is dominated by the slow spreading of the depositing flow.

Rock-ice avalanche modeling

We used two complementary numerical models to test different rheologies and to better constrain main event dynamics. SHALTOP provided an efficient framework to explore the rheological parameter space, whereas a Material Point Method (MPM) model [50, 51] was used to assess the consistency of the resulting flow kinematics in 3D. The MPM model, which solves the mass and momentum balance equations in an Eulerian–Lagrangian framework and resolves the full 3D stress field, captures detachment, internal shearing, and curvature effects beyond the reach of depth-averaged models. We modeled the long-period force histories predicted by each model simulation based on the center of mass trajectories.

The granular flow models were constrained with independent observations: (i) mapped deposit distribution and flow-related features from DEM differencing between 23 May and 29 May 2025 (ETH Zurich product, will be archived on Zenodo and released upon publication) and orthophotos (https://rapidmapping.admin.ch/files/en/pastevents.html) (Figs. 4a-b), and (ii) the inverted seismic force history (Fig. 4k). Model performance was evaluated using four control metrics (refer to Supplementary Material S1): (1) spatial overlap of observed deposit outlines and maximum spatial extent of the simulated deposits (Trimline ratio); (2) Root Mean Squared Error of deposit thickness (Thickness RMSE); (3) normalized cross correlation between the simulated and inverted force histories (Cross-corr); and (4) RMSE of simulated versus inverted force amplitudes after aligning for the maximum cross correlation (Amp RMSE). Because these four metrics possess different units and scales, direct arithmetic combination is invalid. To resolve this, we transformed each raw metric into a z-score, which quantifies standard deviations from the mean performance across all simulations [52]. We assigned a combined weight of 0.7 to the deposit metrics (Trimline ratio and Thickness RMSE) and 0.3 to the seismic metrics (Cross-corr and Amp RMSE). This uneven weighting is justified for two reasons. First, high-resolution topographic differencing provides direct, low-uncertainty measurements, whereas seismic inversions are indirect calculations with accumulated wave-propagation and point-source uncertainties. Second, seismic force history reflects bulk center-of-mass accelerations that are most sensitive to the highly mobile phases of the event. As the mass loses momentum, the signal-to-noise ratio drops, leaving the late-stage depositional dynamics partially unresolved.

We tested different rheologies that represent distinct assumptions and complexities about frictional behavior: a constant friction Coulomb model, a two-parameter

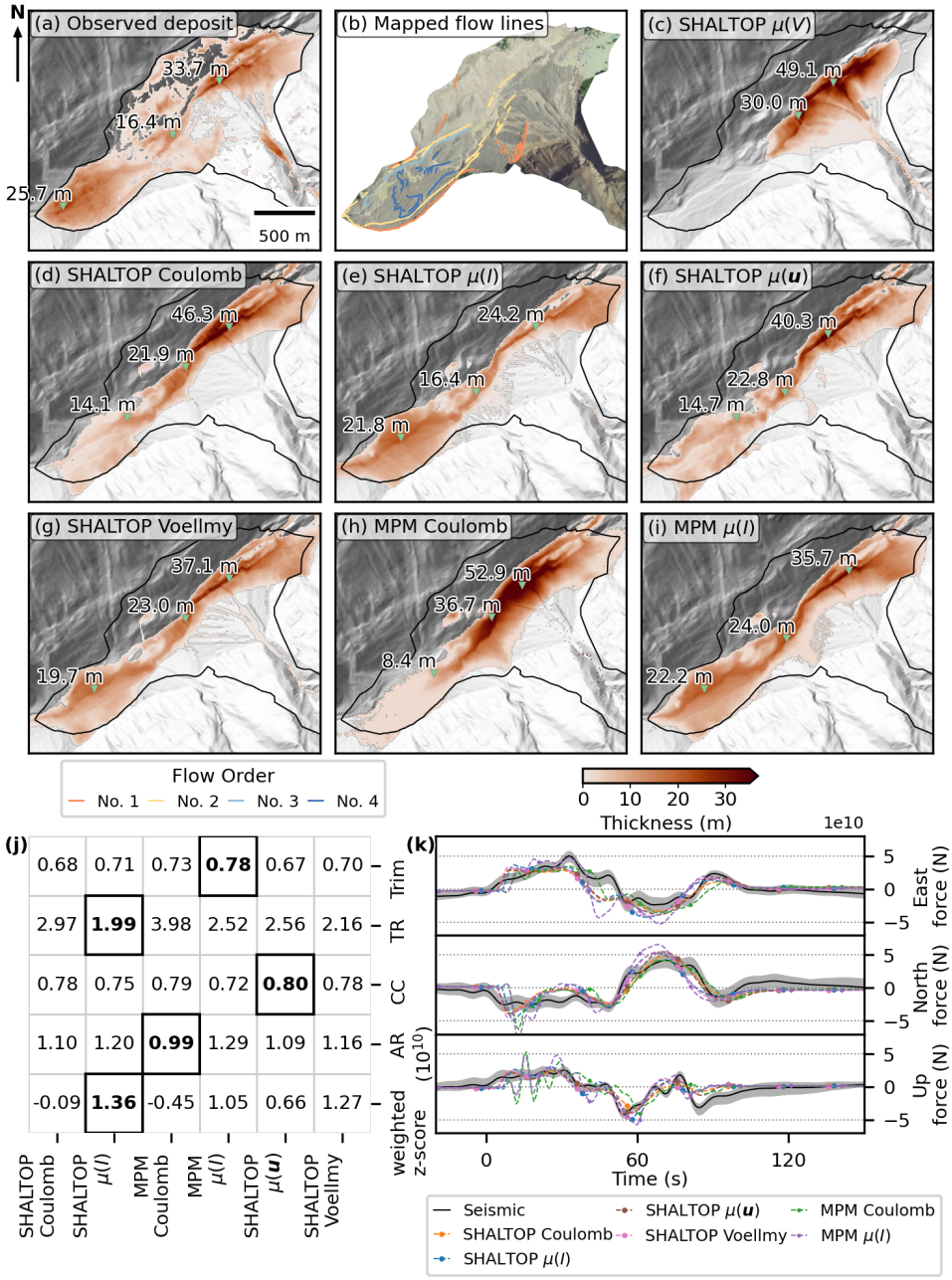

Fig. 4: Comparison of simulation results with deposit and seismic constraints. (a) Observed final deposit thickness. (b) Mapped flow lines based on geomorphological features from post-event (30 May, 2025) aerial view (data sources as in Fig. 1). Colors indicate relative flow sequence, from early (warm colors) to later (cool colors) stages. (c-i) Simulated final deposits from SHALTOP and MPM across different rheologies, each representing the specific simulation that achieved the best overall metric z-scores. Black contours delineate observed deposit outlines. (j) Quantitative comparison of model performance against the final deposit (Trimline ratio(Trim), Thickness RSME(TR)) and seismic force history (Cross-correlation (CC), Amplitude RSME (AR)) as well as the weighted z-score. The best scores among the simulations are bolded. (k) Comparison between the three components of the inverted seismic force and the forces predicted by each model simulation.

Voellmy model, volume-dependent $\mu(V)$ law and laws with variable friction coefficient: velocity ($\mathbf{u}$)-dependent $\mu(\mathbf{u})$ law, and the $\mu(I)$ rheology which depends on the inertial number I [53]. The Coulomb model assumes time-invariant basal resistance. The Voellmy model adds a velocity-squared turbulent drag term to account for increased resistance at high velocity. $\mu(V)$ assumes friction is constant in time and space but varies with event volume, whereas $\mu(\mathbf{u})$ and $\mu(I)$ permit friction to evolve dynamically with flow velocity or inertial number (refer to Supplementary Material S2). Given its well-established integration with seismic force inversion [e.g. 21, 22, 26, 28], we used SHALTOP to perform the primary sensitivity analysis across the listed basal friction laws. Although fully coupled two-phase thermo-hydro-mechanical models could, in principle, describe pore-pressure effects, low ice friction and melt-induced frictional weakening [54–59], these processes, and the associated material parameters, remain difficult to constrain in natural terrain. Therefore, we used the aforementioned one-phase frictional models and treat μ as a parameter that is calibrated to reproduce deposit geometry and seismic data. Because the exceptionally well-documented Blatten event was captured by multiple independent observations, it provides a robust basis for determining the frictional model that best reproduces the data, and constraining its parameters resolving the flow dynamics. The resulting value of μ reflects effective energy dissipation, with lower μ indicating frictional weakening mechanisms that enhance flow mobility.

When calibrating different models to maximize their fit to the observations, the metrics reveal distinct strengths and limitations across different rheologies (Fig. 4j, refer to Supplementary CSV file for the full sensitivity analysis). For a release volume of $\approx 9.3\times10^6$ m^3, the $\mu(V)$ law, empirically fitted on essentially dry landslides, predicts $\delta \approx 16°$ with confidence intervals from 8° to 20° [41]. However, simulations using these values underestimate the observed runout, indicating that the Blatten event was more mobile than expected for dry landslides of comparable size (Fig. 4c). Although Coulomb rheology with $\delta = 8°$ approximates the general runout distance (Fig. 4d), it yields the poorest match for the deposit distribution. The $\mu(\mathbf{u})$ rheology achieves the highest performance against the seismic constraints (Figs. 4j, k). However, it fails to accurately distribute the mass and gives a high Thickness RMSE and the lowest Trimline ratio among the viable models (Figs. 4f, j). The Voellmy rheology provides an intermediate fit but still underestimates lateral spreading (Figs. 4g, j). Only the $\mu(I)$ parameterization (Fig. 4e) captures the late-stage flow surge that produces the thicker deposit distribution at the southwestern margin, where friction decreases toward its lower bound μ_1 during the depositional stage of the simulation (Extended data Fig. 3). We then ran the 3D MPM model for Coulomb and $\mu(I)$ to also simulate the depth-resolved flow kinematics (Figs. 4h, i). For the Coulomb model, the best-fit basal friction angle is $\delta = 11.8°$ for the MPM simulation, which is also near the lower bound of empirical estimates for rock–ice avalanches [41, 60]. However, similar to the SHALTOP results, this constant friction fails to reproduce the observed deposit geometry. For the $\mu(I)$ rheology, the bounds $\delta_1 = 2°$ and $\delta_2 = 16°$ were adopted in SHALTOP and $\delta_1 = 1°$ and $\delta_2 = 16°$ for MPM, where δ_1 and δ_2 denote the lower and upper limits of the $\mu(I)$ law. Also in the MPM simulations, the $\mu(I)$ parameterization provides a better reproduction of the observations than a constant Coulomb friction model.

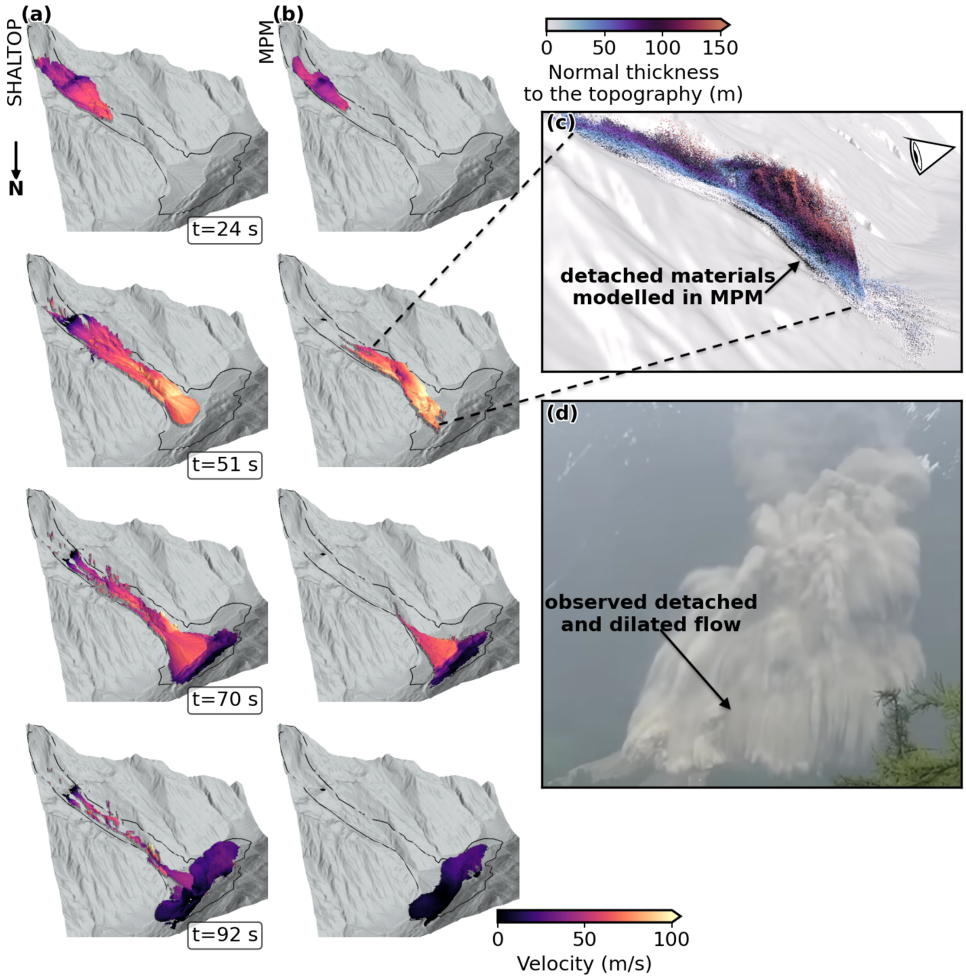

Fig. 5: Snapshots of simulated avalanche dynamics for the $\mu(I)$ rheology. The panels compare the velocity fields predicted by (a) SHALTOP and (b) MPM at key kinematic instances corresponding to the seismic analysis in Fig. 3: acceleration (I, 24 s), gorge transit (II, 51 s), valley-floor collision (III, 70 s), and flow redirection (IV, 92 s). (c) Close-up of the 3D MPM simulation during gorge transit, highlighting detached materials (dashed connectors indicate the view location). The eye symbol marks the approximate viewing direction of the video frame in (d). (d) Frame extracted from video (courtesy of the Canton of Valais) showing the observed detached particle cloud at a similar stage of the avalanche.

Crosscutting levees and lobes on the deposit allow the reconstruction of at least four flow pulses towards the southwest margin of the deposit. We refer to these pulses as flow order 1-4, defined by their relative timing inferred from crosscutting relationships: earlier deposits are overlain and locally incised by later, channelized surges (Fig. 4b). The first pulse determined the maximum southern extent, running ≈80 m (vertical) up in the direction of the source area before flowing farther downstream (flow order 1 in Fig. 4b). Superimposed on this initial deposit are elongated lobes with levees (flow order 2-4 in Fig. 4b) that extend almost 2 km downstream, beyond the village of Blatten. These channelized features incised the initial deposit from the first pulse, indicating a subsequent highly mobile surge. Because a constant-friction rheology fails to capture these complex morphological features, reproducing their extended runout requires the $\mu(I)$ rheology's extreme drop in friction. This drop occurs in several phases (Extended Data Fig. 3). In particular, the near-zero friction required during the late-stage surges ($2°/1°$) strongly indicates the material underwent frictional weakening mechanisms. Beyond ≈92 s, the avalanche's center-of-mass decelerates and the remaining motion transitions into slower, lateral spreading, which produces weaker and more complex force signatures. This complex force history evades the seismic constraints as the low-frequency seismic signals are too weak compared to the background noise.

Comparisons at four representative times (24, 51, 70, 92 s) (Figs. 5a, b) show consistent kinematics between SHALTOP and MPM, with MPM additionally resolving the dilated flow detaching from the topography in the narrow gorge (Figs. 5c, d). The flow front impacts the gorge wall which causes the flow to climb over it. As the valley floor turns concave-downward, the flow partially detaches from the terrain, which is captured explicitly by MPM (Supplementary video 2). Despite the different model dimensionalities, the velocity magnitudes of SHALTOP and MPM remain in close agreement throughout the phases. The consistency between the $\mu(I)$ simulations for SHALTOP and MPM across independent metrics and their best z-score for each model demonstrates that the observed runout and dynamics are only reproduced when δ_1 is exceptionally low ($2°/1°$). This indicates that the effective friction varied significantly throughout the flow with persistent frictional weakening.

Mechanisms driving avalanche mobility

One or several frictional weakening mechanisms must have acted to produce the high mobility of the Blatten rock-ice avalanche [41, 61, 62], extending beyond the physical assumptions of dry granular flows [53]. A primary factor is rock-ice friction reduction. The Blatten rock-ice avalanche involved a total volume of $\approx 9.3 \times 10^6$ m^3, including $\approx 3.0 \times 10^6$ m^3 of ice. The substantial ice content likely favored low-friction interactions within the mixture [44, 63–65]. As demonstrated by Zhou et al. [44], an ice fraction of 32% can reduce the bulk friction angle by approximately 20%. This reduction may explain the best-fit constant Coulomb angles ($8°/11.8°$). However the deposit is not reproduced with constant Coulomb friction; instead, it requires a variable friction as in the $\mu(I)$ law with extreme frictional drop to near-zero lower bounds ($2°/1°$). Therefore, ice content alone cannot fully explain the large observed mobility. During rapid flow, frictional heating likely generated meltwater, which further reduced basal resistance

[60]. In addition, the material deposited on Birch Glacier after the precursory rockfalls originating from the unstable rock-debris mixture on the Kleines Nesthorn may already have been partly wet, which is consistent with the relatively low friction angle ($\delta \approx 20°$) needed to reproduce the seismic energy-duration scaling.

The strong shearing of the rock-ice debris under high normal stress likely also led to dynamic fragmentation, further amplified by strong impact loading against the steep, irregular topography. The fragmentation process could rapidly produce fine particles within the rock-ice mixture and enhance mobility [66]. As shown in Extended data Fig. 3, these expectations agree with our low friction modeled with $\mu(I)$ parameterization during failure, gorge transit, and collision with the counterslope (instances I, II, and III in Fig. 3, respectively).

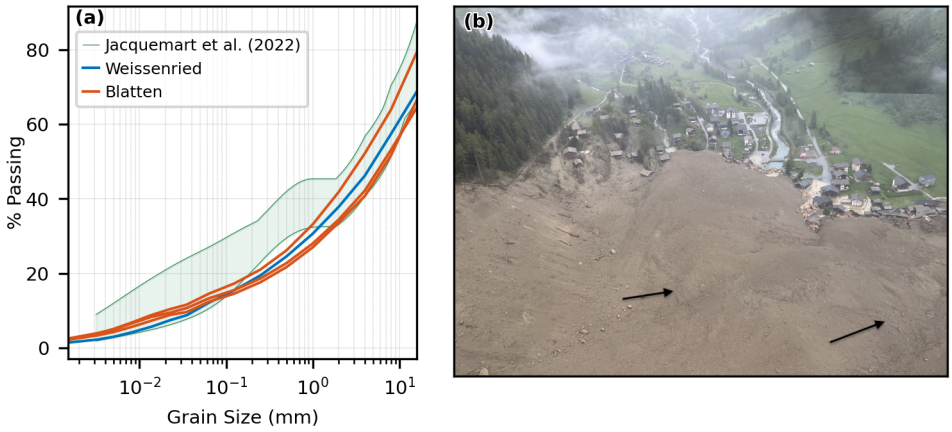

Fig. 6: (a) Grain-size distributions of one sample from the Weissenried counterslope (blue) and three samples from the Blatten main deposit (orange). The collected samples included coarse gravel and small cobbles, up to $\approx$ 5 cm, but excluded larger boulders. The grain-size distribution is compared with data from the Flat Creek glacier detachment deposits reported by Jacquemart et al. [67], rescaled so that the maximum measured grain size corresponds to 5 cm for comparison. (b) Field photograph on 28 May showing the Blatten deposit with darker zones (black arrows) indicating locally wet conditions (ETH Zürich).

Water present in the release mass, or generated during flow through ice melt possibly favored increased pore water pressures in parts of the landslide, which are known to reduce friction by reducing effective stresses in the solid phase [56, 68]. Field surveys conducted shortly after the event documented wet deposits (Fig. 6b), but the hazard posed by potential secondary landslides prevented direct measurements of water content. Consequently, the possible contribution of water to friction reduction can only be inferred from geotechnical analyses of the deposited sediments that we collected later. Grain-size analysis of four samples from the counterslope and main deposit (Fig. 6a) reveal a high fine material content ($\approx$ 15% silt and clay), classifying the

material as well-graded (poorly sorted) gravel with fines, and consistent with the low permeability measured in the deposits ($k_0 \approx 10^{-12}$ m^2) (refer to Methods). These fine particles likely originate from a combination of rock mass from the Kleines Nesthorn and subglacial till from the Birch Glacier. The sediment's texture closely resembles that of another documented fine-rich rock-ice avalanche at Flat Creek (Alaska) [67], with the high fraction of fines originating from subglacial till. Such fine-grained, low-permeability material can sustain high excess pore pressures generated during flow [68]. Impacts with the complex topography induce shearing and compression of the material. This in turn compacts or dilates the granular material that leads to transient increases and decreases of pore water pressures, respectively. These processes may be at the origin of rapid pore pressure generation. Because of the low permeability, these pressures would have dissipated slowly, allowing weakening to persist [54]. This pressure-induced weakening may therefore explain the low friction coefficients, which our granular flow models determine. A two-phase flow model that includes the physics of pore pressure fluctuations can provide more insights, but also requires knowledge of prescribing values for parameters that are both highly uncertain and, in some cases, effectively unmeasurable, yet potentially exert a strong influence on the modeled dynamics [54, 56, 59]. Clear examples include the initial water content, initial dilatancy angle, and permeability evolution during the flow, all of which can substantially affect the magnitude of excess pore pressures generated during motion [59].

Hazard assessment implications

Atmospheric warming and permafrost thaw enhance rockfall activity in high-alpine environments [69–71]. Consequently, rock debris is more likely to deposit onto or mix with glacier ice, which, in turn increases the ice content during catastrophic failures. For the main Blatten rock-ice avalanche, we demonstrated that this effect led to an exceptionally mobile rock-ice avalanche. The involvement of ice also led to lower friction for precursory events, which include failures that deposited on the glacier as well as those that originated from it. Granular friction typically used to model dry rock avalanches did not capture the events' mobility [41].

The integration of oblique aerial photography, geotechnical field characterization of sediments and broadband seismic data is key to constraining and interpreting mobility and therefore the hazard potential of rock-ice avalanches. The involvement of glacial ice has been suggested in runout modeling of historic events [16, 21, 28, 72], and the multi-sensing approach of the present study sets a standard approach to systematic determination of effective friction. On the other hand, for hazard management of future events or ongoing mass movement activity resulting from rock instability, our seismic signal classification also provides a useful tool. The unsupervised signal clustering [34], combined with granular flow modelling, can identify telltale event types and quantify volumes associated with slope failures that can be specifically monitored in case other observations are unavailable. In our case, this was possible with an earthquake monitoring seismometer providing real-time mass movement detections at a distance of ≈5 km from the Blatten area. As machine learning algorithms continue

to enhance seismic signal processing, streaming seismometers will play an increasingly important role in slope monitoring and can provide information on precursory events as soon as an instability is identified. This is already now possible, whereas comprehensive identification of mass movement signals in an entire seismic network may not yet be feasible as a result of limitations in computational power, training data and algorithm transferability. Importantly, in our case, a closer analysis of the precursory rockfall activity already pointed out the need to employ low friction angles and thus expect high mobility of failing masses in the main event.

A more physics-based multi-phase model could pinpoint the processes behind friction reduction, which may include liquefaction, fragmentation and rock-ice friction reduction among others [54–59]. However, epistemic uncertainty in the initial water content of the release mass and in key geomechanical parameters like material dilatancy precluded the use of more complex thermo-hydro-mechanical models. Nevertheless, our results show that both depth-averaged flow models and 3D granular models capture increased runout mobility when forced and interpreted with pivotal data. The combination of seismology, direct geomorphological observations, geotechnical experiments and granular flow models therefore holds great potential in understanding previous and managing future hazardous mass movements.

Methods

Seismic event clustering and volume estimation

We applied a self-supervised learning workflow [34] that combines representation learning with iterative clustering to identify and characterize slope-seismic activity preceding the 28 May 2025 collapse. At a high level, this algorithm relies on grouping signals with similar time-frequency characteristics, such as spectral distribution, signal envelope, and duration. This enables the model to distinguish impulsive signatures of discrete rockfalls from the emergent patterns of complex mass movements. The continuous vertical component (HHZ) waveform at station LAUCH, recorded between 1 January and 1 June 2025, was segmented into 180 s windows and converted into dual-panel images (spectrogram and high-pass filtered waveform > 1 Hz), yielding 73,387 images. A BYOL-based self-supervised model [73] encoded these images into 512-dimensional latent representations. The embeddings were first partitioned using k-means clustering (3,000 centroids, 300 iterations) and then hierarchically merged based on an inconsistency coefficient of 3, resulting in 236 distinct signal clusters. Manual inspection and refined arrival-time picking yielded a high-confidence catalog of 2,265 events, of which 17 clusters ($\approx$700 events) showed clear pre-failure acceleration.

Event volumes were inferred from seismic energy and signal duration using the empirical scaling framework of Hibert et al. [29], Levy et al. [30], Farin et al. [36]. Event durations were determined manually. For the seismic records, start and end times were picked based on the signal-to-noise ratio and spectrogram characteristics. For the SHALTOP simulations, similar to the approach by Hibert et al. [29], the end time was defined as the moment when no significant change was observed in the potential energy time series. Following the methodology of Hibert et al. [29] and Vilajosana et al. [74],

seismic energy was calculated by assuming a ground density of 2,100 kg/m^3, a seismic wave velocity of 2,500 m/s, a quality factor $Q = 100$, and a central frequency of 5 Hz.

To ensure realistic release dynamics in the SHALTOP simulations, the initial failure masses were reconstructed by distributing the predefined volumes across the source areas using a slope-weighted distribution. The volume assigned to each pixel was weighted inversely to the local terrain slope, allowing more mass to be allocated to flatter regions. The final basal failure surface was generated by subtracting these derived vertical depths from the pre-event DEM.

As introduced in the main text, the recorded seismic energy E_s is empirically linked to the loss of potential energy E_p [29]. Assuming proportionality between E_s and E_p via their respective power-law scalings with duration ($E_s = \alpha t_s^{\beta}$ and $E_p = \alpha' t_p^{\beta'}$ where $t_S = t_p$), we derived E_p from the energy conversion ratio $R_{ps} = \frac{E_p}{E_s}$, which is calibrated on the granular flow simulations (refer to Fig. 2c,d).

From the seismic recording, we can only measure the radiated seismic energy E_s. To relate E_s to the actual release volume (V_{real}), we rely on the relation $E_p = \rho g H V$, where ρ is the bulk density and H the mean fall height [29]. From the SHALTOP simulations, we extract both the explicitly known input volumes (V_{sim}) and their corresponding simulated kinematic potential energy ($E_{p,sim}$, which accounts for gHV) for the two families. Using these outputs, we establish a linear proportionality factor, R_{E_pV}, between $E_{p,sim}$ and V_{sim} by assuming a constant density ρ. By bridging the seismic observations and the granular flow simulations, we calculate the real event volume as $V_{real} \approx \frac{R_{ps} E_s}{R_{E_pV}}$.

We account for the substantial parameter uncertainties propagated through this approximation. Because the empirical power-law fits for E_s and E_p are not exactly with the same slope, the energy conversion ratio R_{ps} varies across the duration range. Furthermore, the source density ρ varies for each event. To establish a confidence envelope for the cumulative mass wasting volume, we calculated upper and lower volume bounds by varying these physical and empirical parameters. The energy ratio bounds ($R_{ps,min}$, $R_{ps,max}$) were extracted from the spread between the two fitted power-law lines for E_s and E_p. For Family 1 (rockfalls), we assumed a source mass density ρ from 2,200 to 2,700 $\mathrm{kg\,m^{-3}}$, which reflects the variation between highly fractured rock mass and intact bedrock [75]. For Family 2 (small rock-ice avalanches), the source density relies on the volumetric ice fraction. Treating these failures as binary mixtures of glacier ice and rock debris, we assumed an ice fraction variation between 30% and 70%. Using constituent densities of 917 [76] for ice and 2,500 $\mathrm{kg\,m^{-3}}$ for rock yields a ρ uncertainty range of 1,430 to 2,041 $\mathrm{kg\,m^{-3}}$. The final upper and lower volume bounds were computed using the extreme combinations of R_{ps}, ρ, by the two boundaries.

Seismic force inversion and metrics calculation

We inverted the long-period (15–180 s) seismic waveforms from broadband stations between 33 km and 110 km from the source to reconstruct the time-dependent center-of-mass force history. The point force was located at (46.40°, 7.84°). We omitted station LAUCH from the analysis because its close proximity to the event (5 km) violates

the assumptions of the method. Other stations were omitted on a case-by-case basis if their data quality was clearly poor (e.g. excessive long-period noise). Data were detrended, tapered, corrected for instrument response to displacement (including a cosine taper filter with corners at 15 and 180 s), again detrended using a second-order spline to remove very-long-period artifacts, and again tapered. The inversion followed the *lsforce* approach [45, 46] using the following parameters: `iasp91_2s` Earth model, no zero start imposition, no add-to-zero constraint, regularization parameter $\alpha = 1.5\times10^{-17}$, and Tikhonov ratios (0.4, 0, 0.6). Channels with remaining substantial very-long-period noise were down-weighted. The result achieves a variance reduction (VR) of 85%. Uncertainty was quantified via a jackknife scheme with 20 iterations, each dropping half of the input stations. VR ranged from 81–91% with a median of 86%, indicating stable solutions across station subsets. The seismically derived and numerical landslide model-derived forces were compared using four quantitative metrics: (1) deposit overlap (Trimline ratio), (2) deposit-thickness RMSE, (3) force cross-correlation, and (4) amplitude RMSE (refer to Supplementary Material S1. and Eqs. S1–S4).

Depth-averaged granular flow modeling

SHALTOP [38, 77] solves the depth-averaged equations for dry granular flows on a complex topography [17, 22, 39–42]. The equations are depth-averaged along the direction normal to the topography to apply the shallow flow approximation accurately. Furthermore, SHALTOP accurately accounts for the complex topography curvature, which affects the dynamics and deposition of granular flows [42]. SHALTOP's strengths lie in the small number of parameters involved and its extensive validation through a series of laboratory experiments and field observations, including seismic data [16, 21, 27, 28, 38–41, 62]. The model can handle different rheologies, including a Coulomb-type friction law with a constant or variable effective friction coefficient μ.

Simulations of dry landslides and rock avalanches show that the values of the friction coefficients in the models have to be very small to reproduce the runout distance and the dynamics of events with large volume [41, 78]. These values are thus empirical. This increase of flow mobility with increasing volume remains an open key question. To obtain a first estimate of a typical friction coefficient with a volume $V \approx 9.3\times10^6$ m^3, we used the $\mu(V)$ law, where V is the avalanche volume, derived from numerical back-analyses of natural dry rock and debris avalanches using a constant Coulomb friction law [41]

$$\mu(V) = V^{-0.0774}. \tag{1}$$

Other tested laws include constant Coulomb, velocity-weakening [41], Voellmy, and rate-dependent $\mu(I)$ rheologies. For the main avalanche, best-fit parameters of $\mu(I)$ were $\mu_1 = 0.05$, $\mu_2 = 0.23$, $\varphi = 0.7$, $d = 0.3$ m, and $I_0 = 0.279$. Parameter sensitivity and full equations are given in Supplementary Material S2.

3D MPM granular flow modeling

To assess 3D effects, we conduct 3D continuum simulations of the rock-ice avalanche using MPM. This numerical method, typically attributed to Sulsky et al. [79], allows

for the capturing of solid-fluid transitions and naturally handles free surface dynamics. In an elasto-viscoplastic framework based on the multiplicative decomposition of the deformation gradient into an elastic and viscoplastic part, we formulate a Drucker–Prager model [80] which depends on the inertial number. As such, the $\mu(I)$-rheology can be recovered under flow conditions. For the main avalanche, best-fit parameters of $\mu(I)$ were $\mu_1 = 0.02$, $\mu_2 = 0.28$, $\varphi = 0.7$, $d = 0.3$ m, and $I_0 = 0.01$.

This versatile model enables the simulation of both cohesionless and cohesive granular flows, including snow, rock, or ice avalanches, as well as landslides. The details of the elasto-viscoplastic framework are comprehensively presented in Blatny et al. [51], Blatny and Gaume [81], which also introduces more advanced constitutive laws that may account for dilatancy and compressibility effects. Full constitutive details are provided in Supplementary Material S3. Following the framework of [82], the 3D simulation results are in this article converted into depth-averaged variables for 2D visualization and metric evaluation.

Geotechnical field investigation

Four sediment samples were collected from the uppermost sediment layer of the deposits, both on the counterslope and at the main deposit (Fig. 1b). Grain-size distribution (GSD) was determined on a weight basis using dry sieving, wet sieving, and hydrometer analysis to characterize the fraction finer than 16 mm, following the Swiss Norms [83]. The collected field samples also contained material coarser than 16 mm (coarse gravel and cobbles), which was proportionally scaled and included in the final GSD (Fig. 6a). Larger boulders were observed on site, but could not be incorporated into a complete GSD. Visual observations indicate (Extended data Fig. 4), however, that these boulders are embedded within a matrix-supported mixture of cobbles, gravel, sand and fines. This indicates that landslide behavior was governed primarily by this sediment matrix rather than by interactions among boulders. Samples from the counterslope and the main deposit show similar GSDs, though the counterslope was visually richer in boulders, indicating preferential coarse deposition there while finer, more mobile fractions continued downstream.

Field-saturated hydraulic conductivity (K_{fs}) was measured in-situ at the southwestern margin of the deposits (Fig. 1b) using the METER SATURO dual-head infiltrometer [84, 85]. Three tests yielded relatively low values (average $K_{fs} = 1.5 \times 10^{-5}$ m/s) and high variability ($\sigma_{fs} = 1.5 \times 10^{-5}$ m/s). Nonetheless, a simple estimate of the saturated hydraulic conductivity using Hazen's empirical relation, based on mean $D_{10} = 0.033$ mm (the grain diameter at 10% passing, extracted from the measured GSDs), yielded a comparable value ($K_s = 1.1 \times 10^{-5}$ m/s), which is within the range of the SATURO measurements. Converting to intrinsic permeability using $k_0 = K_{fs}\eta_w\gamma_w^{-1}$, where γ_w is the unit weight of water and $\eta_w = 10^{-3}$ Pa $\cdot$ s its viscosity, gives $k_0 \approx 10^{-12}$ m^2.

Extended data

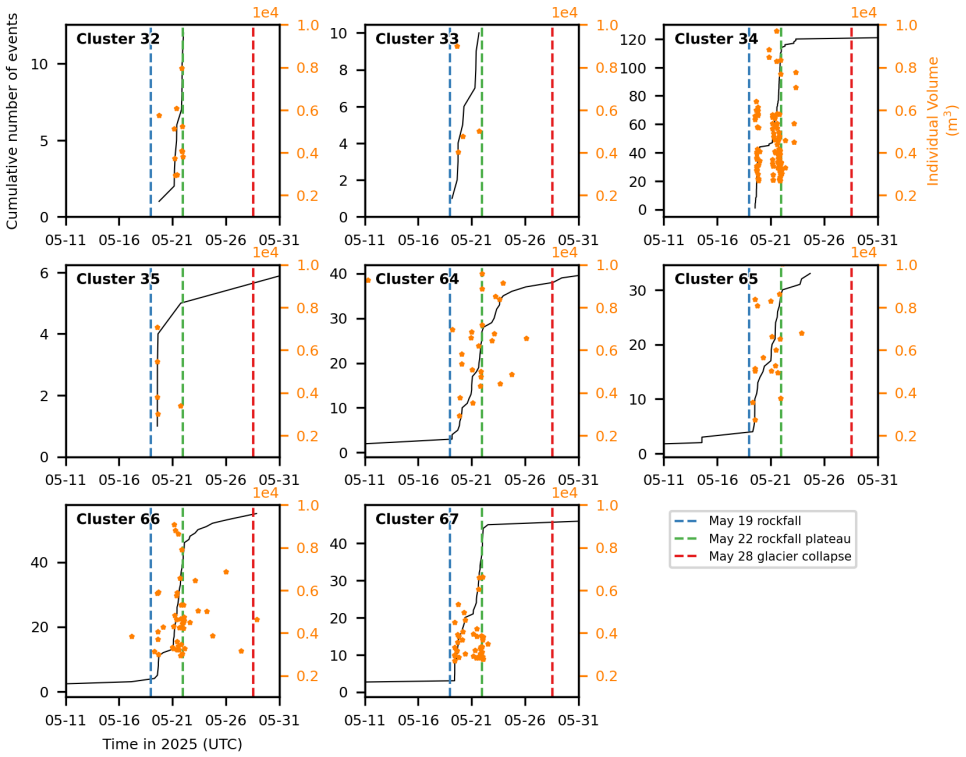

Extended Data Fig. 1 — Temporal evolution of Family 1 from 11 May to 30 May. Cumulative number of events (black) and estimated individual volumes (orange) for clusters from Family 1. Vertical dashed lines indicate the onset of major phases: May 19 (rockfall acceleration), May 22 (rockfall plateau), and May 28 (main glacier collapse).

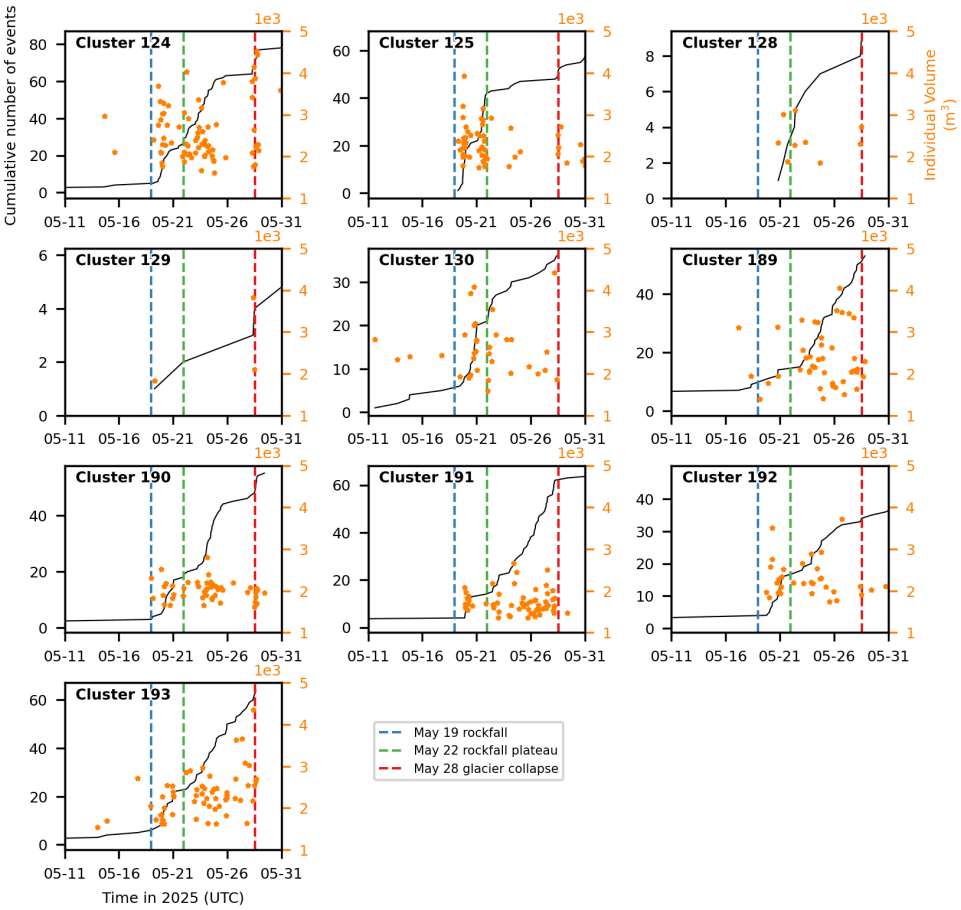

Extended Data Fig. 2 — Temporal evolution of Family 2 from 11 May to 30 May. Cumulative number of events (black) and estimated individual volumes (orange) for clusters from Family 2. Vertical dashed lines mark the same key phases as in Extended Data Fig. 1.

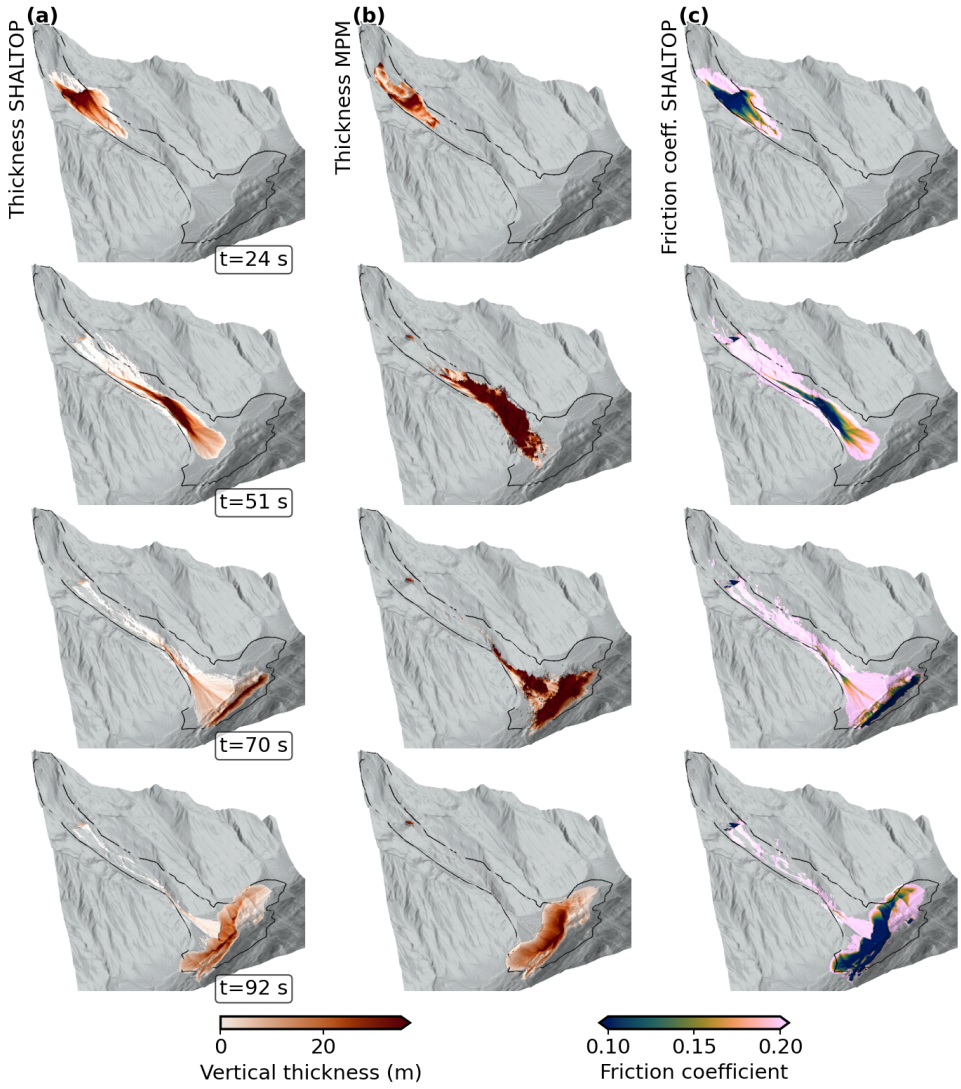

Extended Data Fig. 3 — Snapshots of simulated avalanche dynamics for the $\mu(I)$ rheology (topographic data based on post-event (29 May 2025) DEM). Panels show the evolution of vertical thickness from (a) the SHALlow water depth-averaged numerical model (SHALTOP) and (b) Material Point Method model (MPM), and the corresponding apparent friction coefficient (c) from SHALTOP at key kinematic instances corresponding to the seismic analysis in Fig. 3: acceleration (I, 24 s), gorge transit (II, 51 s), valley-floor collision (III, 70 s), and flow redirection (IV, 92 s).

Extended Data Fig. 4 — Field photographs of the Birch Glacier avalanche deposit (ETH Zürich). (a) Sampling of the main deposit surface. (b) Close-up view of the matrix-supported texture, where coarse fragments are partially buried in fine material.

Acknowledgements. J.K., F.W. and A.M. have received funding from the European Union's Horizon 2021 research and innovation program (EnvSeis) under grant agreement No. 101073148. A.L. acknowledges support from CNES for the STERREO project. L.B. acknowledges support from the Swiss National Science Foundation (grant number P500PT_230265). C.H. and J.R. have received funding by the Agence Nationale de la Recherche (ANR) - Projet ANR-20-CE01-0006 "HighLand: Landslides and Climate Change in highly Sensible Environments: Seismology, Earth Observation and Artificial Intelligence." Authors are grateful to Ralf Herzog (ETHZ) for performing grain size distribution analysis of Blatten sediments, and thank the Albert Lück-Stiftung for their financial support. We gratefully acknowledge the constructive feedback provided by Katy Barnhart during the U.S. Geological Survey (USGS) internal review process, which significantly improved the quality of this manuscript. Any use of trade, firm, or product names is for descriptive purposes only and does not imply endorsement by the U.S. Government.

Declarations

- Conflict of interest/Competing interests (check journal-specific guidelines for which heading to use)
  The authors declare that they have no conflict of interest.
- Data availability
  All seismic waveform data used in this study are publicly available from the Swiss Seismological Service (SED) at http://www.seismo.ethz.ch/en/knowledge/earthquake-data-and-analysis-tools/waveform-data/. The derived datasets, including geomorphological maps, digital elevation models, and geotechnical measurements, will be archived upon review together with the codes.
- Code availability
  All codes used for post-processing, model evaluation, and figure generation will be made openly available upon review procedure on Zenodo. The self-supervised seismic clustering algorithm is available on GitLab at https://gitlab.com/eost/seis-clust-ssl. The *lsforce* inversion code can be accessed at https://code.usgs.gov/ghsc/lhp/lsforce, the SHALTOP model at https://zenodo.org/records/10964107, and the MPM framework at https://github.com/larsblatny/matter/.
- Author contribution
  Conceptualization: J.K., A.L., F.W., A.M., J.G., K.A., C.H., L.T., M.D.
  Data curation: J.K., F.W., J.G., H.V., M.J., D.F., A.L., K.A., C.H., L.T.,
  Data Investigation: J.K., A.L., A.M., J.G., K.A., C.H., L.T., H.V., M.D., M.J.
  Software: A.M., J.G., A.L., K.A., C.H., L.T., J.K., M.P., L.B., M.L.K., J.R.,
  Supervision: F.W., A.L., A.M., J.G.
  Validation: J.K., A.L., A.M., J.G., K.A., C.H., L.T., H.V., M.J.
  Visualization: J.K., A.L., J.G., K.A., C.H., L.T., H.V., M.J
  Writing - original draft: J.K., A.L., A.M., J.G., F.W., H.V., C.H., M.J., L.B.

References

[1] Shugar, D.H., Jacquemart, M., Shean, D., Bhushan, S., Upadhyay, K., Sattar, A., Schwanghart, W., McBride, S., Vries, M.V.W., Mergili, M., *et al.*: A massive rock and ice avalanche caused the 2021 disaster at chamoli, indian himalaya. Science **373**(6552), 300–306 (2021) https://doi.org/10.1126/science.abh4455 https://www.science.org/doi/pdf/10.1126/science.abh4455

[2] Svennevig, K., Hicks, S.P., Forbriger, T., Lecocq, T., Widmer Schnidrig, R., Mangeney, A., Hibert, C., Korsgaard, N.J., Lucas, A., Satriano, C., *et al.*: A rockslide-generated tsunami in a greenland fjord rang earth for 9 days. Science **385**(6714), 1196–1205 (2024) https://doi.org/10.1126/science.adm9247

[3] Yanites, B.J., Clark, M.K., Roering, J.J., West, A.J., Zekkos, D., Baldwin, J.W., Cerovski-Darriau, C., Gallen, S.F., Horton, D.E., Kirby, E., Leshchinsky, B.A., Mason, H.B., Moon, S., Barnhart, K.R., Booth, A., Czuba, J.A., McCoy, S., McGuire, L., Pfeiffer, A., Pierce, J.: Cascading land surface hazards as a nexus in the earth system. Science **388**(6754), 9559 (2025) https://doi.org/10.1126/science.adp9559 https://www.science.org/doi/pdf/10.1126/science.adp9559

[4] Cook, K.L., Rekapalli, R., Dietze, M., Pilz, M., Cesca, S., Rao, N.P., Srinagesh, D., Paul, H., Metz, M., Mandal, P., Suresh, G., Cotton, F., Tiwari, V.M., Hovius, N.: Detection and potential early warning of catastrophic flow events with regional seismic networks. Science **374**(6563), 87–92 (2021) https://doi.org/10.1126/science.abj1227

[5] Li, G., West, A.J., Densmore, A.L., Hammond, D.E., Jin, Z., Zhang, F., Wang, J., Hilton, R.G.: Connectivity of earthquake-triggered landslides with the fluvial network: Implications for landslide sediment transport after the 2008 wenchuan earthquake. Journal of Geophysical Research: Earth Surface **121**(4), 703–724 (2016) https://doi.org/10.1002/2015JF003718 https://agupubs.onlinelibrary.wiley.com/doi/pdf/10.1002/2015JF003718

[6] Kääb, A., Jacquemart, M., Gilbert, A., Leinss, S., Girod, L., Huggel, C., Falaschi, D., Ugalde, F., Petrakov, D., Chernomorets, S., Dokukin, M., Paul, F., Gascoin, S., Berthier, E., Kargel, J.S.: Sudden large-volume detachments of low-angle mountain glaciers – more frequent than thought? The Cryosphere **15**(4), 1751–1785 (2021) https://doi.org/10.5194/tc-15-1751-2021

[7] Jacquemart, M., Weber, S., Chiarle, M., Chmiel, M., Cicoira, A., Corona, C., Eckert, N., Gaume, J., Giacona, F., Hirschberg, J., Kaitna, R., Magnin, F., Mayer, S., Moos, C., van Herwijnen, A., Stoffel, M.: Detecting the impact of climate change on alpine mass movements in observational records from the european alps. Earth-Science Reviews **258**, 104886 (2024) https://doi.org/10.1016/j.earscirev.2024.104886

[8] Svennevig, K., Hicks, S.P., Forbriger, T., Lecocq, T., Widmer-Schnidrig, R., Mangeney, A., Hibert, C., Korsgaard, N.J., Lucas, A., Satriano, C., Anthony, R.E., Mordret, A., Schippkus, S., Rysgaard, S., Boone, W., Gibbons, S.J., Cook, K.L., Glimsdal, S., Løvholt, F., Noten, K.V., Assink, J.D., Marboeuf, A., Lomax, A., Vanneste, K., Taira, T., Spagnolo, M., Plaen, R.D., Koelemeijer, P., Ebeling, C., Cannata, A., Harcourt, W.D., Cornwell, D.G., Caudron, C., Poli, P., Bernard, P., Larose, E., Stutzmann, E., Voss, P.H., Lund, B., Cannavo, F., Castro-Díaz, M.J., Chaves, E., Dahl-Jensen, T., Dias, N.D.P., Déprez, A., Develter, R., Dreger, D., Evers, L.G., Fernández-Nieto, E.D., Ferreira, A.M.G., Funning, G., Gabriel, A.-A., Hendrickx, M., Kafka, A.L., Keiding, M., Kerby, J., Khan, S.A., Dideriksen, A.K., Lamb, O.D., Larsen, T.B., Lipovsky, B., Magdalena, I., Malet, J.-P., Myrup, M., Rivera, L., Ruiz-Castillo, E., Wetter, S., Wirtz, B.: A rockslide-generated tsunami in a greenland fjord rang earth for 9 days. Science **385**(6714), 1196–1205 (2024) https://doi.org/10.1126/science.adm9247 https://www.science.org/doi/pdf/10.1126/science.adm9247

[9] Li, Y., Cui, Y., Hu, X., Lu, Z., Guo, J., Wang, Y., Wang, H., Wang, S., Zhou, X.: Glacier retreat in eastern himalaya drives catastrophic glacier hazard chain. Geophysical Research Letters **51**(8), 2024–108202 (2024) https://doi.org/10.1029/2024GL108202 https://agupubs.onlinelibrary.wiley.com/doi/pdf/10.1029/2024GL108202. e2024GL108202 2024GL108202

[10] Federal Office for the Environment (FOEN/BAFU): Natural Hazards: In Brief. Accessed 2025-09-10. https://www.bafu.admin.ch/bafu/en/home/topics/natural-hazards/in-brief.html

[11] Petley, D.: The 28 April 2025 Glacial Outburst Flood (GLOF) / landslide at Vallunaraju in Peru. https://eos.org/thelandslideblog/vallunaraju-1 (28 April 2025)

[12] Poli, P.: Creep and slip: Seismic precursors to the nuugaatsiaq landslide (greenland). Geophysical Research Letters **44**(17), 8832–8836 (2017) https://doi.org/10.1002/2017GL075039 https://agupubs.onlinelibrary.wiley.com/doi/pdf/10.1002/2017GL075039

[13] Lacroix, P., Bièvre, G., Pathier, E., Kniess, U., Jongmans, D.: Use of sentinel-2 images for the detection of precursory motions before landslide failures. Remote Sensing of Environment **215**, 507–516 (2018) https://doi.org/10.1016/j.rse.2018.03.042

[14] Paitz, P., Lindner, N., Edme, P., Huguenin, P., Hohl, M., Sovilla, B., Walter, F., Fichtner, A.: Phenomenology of avalanche recordings from distributed acoustic sensing. Journal of Geophysical Research: Earth Surface **128**(5), 2022–007011 (2023) https://doi.org/10.1029/2022JF007011 https://agupubs.onlinelibrary.wiley.com/doi/pdf/10.1029/2022JF007011. e2022JF007011 2022JF007011

[15] Kang, J., Walter, F., Paitz, P., Aichele, J., Edme, P., Meier, L., Fichtner, A.: Automatic monitoring of rock-slope failures using distributed acoustic sensing and semi-supervised learning. Geophysical Research Letters **51**(19), 2024–110672 (2024) https://doi.org/10.1029/2024GL110672 https://agupubs.onlinelibrary.wiley.com/doi/pdf/10.1029/2024GL110672. e2024GL110672 2024GL110672

[16] Favreau, P., Mangeney, A., Lucas, A., Crosta, G., Bouchut, F.: Numerical modeling of landquakes. Geophysical Research Letters **37**, 15305 (2010) https://doi.org/10.1029/2010GL043512

[17] Peruzzetto, M., Levy, C., Thiery, Y., Grandjean, G., Mangeney, A., Lejeune, A.-M., Nachbaur, A., Legendre, Y., Vittecoq, B., Saurel, J.-M., Clouard, V., Dewez, T., Fontaine, F.R., Mergili, M., Lagarde, S., Komorowski, J.-C., Le Friant, A., Lemarchand, A.: Simplified simulation of rock avalanches and subsequent debris flows with a single thin-layer model: Application to the Prêcheur river (Martinique, Lesser Antilles). Engineering Geology **296**, 106457 (2022) https://doi.org/10.1016/j.enggeo.2021.106457

[18] Hungr, O.: Entrainment of debris in rock avalanches : An analysis of a long runout mechanism. GSA Bulletin **116**(9/10), 1240–1252 (2004) https://doi.org/10.1130/B25362.1

[19] Iverson, R.M., George, D.L., Allstadt, K., Reid, M.E., Collins, B.D., Vallance, J.W., Schilling, S.P., Godt, J.W., Cannon, C.M., Magirl, C.S., Baum, R.L., Coe, J.A., Schulz, W.H., Bower, J.B.: Landslide mobility and hazards: implications of the 2014 oso disaster. Earth and Planetary Science Letters **412**, 197–208 (2015) https://doi.org/10.1016/j.epsl.2014.12.020

[20] McDougall, S.: 2014 canadian geotechnical colloquium: Landslide runout analysis — current practice and challenges. Canadian Geotechnical Journal **54**(5), 605–620 (2017) https://doi.org/10.1139/cgj-2016-0104

[21] Moretti, L., Mangeney, A., Walter, F., Capdeville, Y., Bodin, T., Stutzmann, E., Le Friant, A.: Constraining landslide characteristics with bayesian inversion of field and seismic data. Geophysical Journal International **221**(2), 1341–1348 (2020) https://doi.org/10.1093/gji/ggaa056

[22] Moretti, L., Mangeney, A., Capdeville, Y., Stutzmann, E., Bouchut, F.: Numerical modeling of the mount steller landslide flow history and of the generated long-period seismic waves. Geophysical Research Letters **39**, 16402 (2012) https://doi.org/10.1029/2012GL052511

[23] Ekström, G., Stark, C.P.: Simple scaling of catastrophic landslide dynamics. Science **339**(6126), 1416–1419 (2013) https://doi.org/10.1126/science.1232887

[24] Allstadt, K.: Extracting source characteristics and dynamics of the august 2010

mount meager landslide from broadband seismograms. Journal of Geophysical Research: Earth Surface **118**(3), 1472–1490 (2013) https://doi.org/10.1002/jgrf.20110 https://agupubs.onlinelibrary.wiley.com/doi/pdf/10.1002/jgrf.20110

[25] Hibert, C., Ekström, G., Stark, C.P.: Dynamics of the bingham canyon mine landslides from seismic signal analysis. Geophysical Research Letters **41**, 4535–4541 (2014) https://doi.org/10.1002/2014GL060592

[26] Walter, F., Amann, F., Kos, A., Kenner, R., Phillips, M., de Preux, A., Huss, M., Tognacca, C., Clinton, J., Diehl, T., Bonanomi, Y.: Direct observations of a three million cubic meter rock-slope collapse with almost immediate initiation of ensuing debris flows. Geomorphology **351**, 106933 (2020) https://doi.org/10.1016/j.geomorph.2019.106933

[27] Yamada, M., Mangeney, A., Matsushi, Y., Moretti, L.: Estimation of dynamic friction of the akatani landslide from seismic waveform inversion and numerical simulation. Geophysical Journal International **206**(3), 1479–1486 (2016) https://doi.org/10.1093/gji/ggw216

[28] Moretti, L., Mangeney, A., Allstadt, K., Capdeville, Y., Stutzmann, E.: Numerical modeling of the mount meager landslide constrained by its force history derived from seismic data. Journal of Geophysical Research: Solid Earth **120**, 2579–2599 (2015) https://doi.org/10.1002/2014JB011426

[29] Hibert, C., Mangeney, A., Grandjean, G., Shapiro, N.M.: Slope instabilities in dolomieu crater, Réunion island: From seismic signals to rockfall characteristics. Journal of Geophysical Research: Earth Surface **116**(F4), 04032 (2011) https://doi.org/10.1029/2011JF002038

[30] Levy, C., Mangeney, A., Bonilla, F., Hibert, C., Calder, E.S., Smith, P.J.: Friction weakening in granular flows deduced from seismic records at the soufrière hills volcano, montserrat. Journal of Geophysical Research: Solid Earth **120**(11), 7536–7557 (2015) https://doi.org/10.1002/2015JB012151 https://agupubs.onlinelibrary.wiley.com/doi/pdf/10.1002/2015JB012151

[31] Farinotti, D., Huss, M., Jacquemart, M., Werder, M., Walden, J., Knutti, R., Seneviratne, S., Kenner, R., Nötzli, J., Phillips, M., Glagliardini, O., Schuler, T.: Fact sheet for the now-collapsed Birchgletscher, Switzerland. Technical Report 88028-VAW-2025-07, ETH Zurich Laboratory of Hydraulics, Hydrology and Glaciology VAW, and Swiss Federal Institute for Forest, Snow and Landscape Research (WSL), Zurich (June 2025)

[32] News, S.: Lonza steigt +++ Gampel/Steg sollen sich auf Räumung vorbereiten (2025). https://www.srf.ch/news/schweiz/dorf-blatten-verschuettet-lonza-steigt-gampel-steg-sollen-sich-auf-raeumung-vorbereiten

[33] Swiss Seismological Service: Mass Movements (2025). http://www.seismo.ethz.ch/en/earthquakes/switzerland/massmovements/

[34] Rimpot, J., Hibert, C., Malet, J.-P., Forestier, G., Weber, J.: Self-supervised learning based clustering workflow for exploring seismological data from dense networks. Journal of Geophysical Research: Machine Learning and Computation **2**(4), 2025–000958 (2025) https://doi.org/10.1029/2025JH000958

[35] Durand, V., Mangeney, A., Bernard, P., Jia, X., Bonilla, F., Satriano, C., Saurel, J.-M., Aissaoui, E.M., Peltier, A., Ferrazzini, V., Kowalski, P., Lauret, F., Brunet, C., Hibert, C.: Repetitive small seismicity coupled with rainfall can trigger large slope instabilities on metastable volcanic edifices. Communications Earth & Environment **4**(1), 383 (2023) https://doi.org/10.1038/s43247-023-00996-y

[36] Farin, M., Mangeney, A., Rosny, J., Toussaint, R., Trinh, P.-T.: Link between the dynamics of granular flows and the generated seismic signal: Insights from laboratory experiments. Journal of Geophysical Research: Earth Surface **123**(6), 1407–1429 (2018) https://doi.org/10.1029/2017JF004296 https://agupubs.onlinelibrary.wiley.com/doi/pdf/10.1029/2017JF004296

[37] Mangeney-Castelnau, A., Vilotte, J.-P., Bristeau, M.O., Perthame, B., Bouchut, F., Simeoni, C., Yerneni, S.: Numerical modeling of avalanches based on saint-venant equations using a kinetic scheme. Journal of Geophysical Research: Solid Earth **108**(B11), 2527 (2003) https://doi.org/10.1029/2002JB002024

[38] Mangeney-Castelnau, A., Bouchut, F., Vilotte, J.P., Lajeunesse, E., Aubertin, A., Pirulli, M.: On the use of Saint Venant equations to simulate the spreading of a granular mass: Numerical simulation of granular spreading. Journal of Geophysical Research: Solid Earth **110**(B9), 09103 (2005) https://doi.org/10.1029/2004JB003161

[39] Lucas, A., Mangeney, A.: Mobility and topographic effects for large Valles Marineris landslides on Mars. Geophysical Research Letters **34**(10), 10201 (2007) https://doi.org/10.1029/2007GL029835

[40] Lucas, A., Mangeney, A., Mège, D., Bouchut, F.: Influence of the scar geometry on landslide dynamics and deposits: Application to Martian landslides. Journal of Geophysical Research **116**(E10) (2011) https://doi.org/10.1029/2011JE003803

[41] Lucas, A., Mangeney, A., Ampuero, J.P.: Frictional velocity-weakening in landslides on earth and on other planetary bodies. Nature Communications **5**(1), 3417 (2014) https://doi.org/10.1038/ncomms4417

[42] Peruzzetto, M., Mangeney, A., Bouchut, F., Grandjean, G., Levy, C., Thiery, Y., Lucas, A.: Topography curvature effects in thin-layer models for gravity-driven flows without bed erosion. Journal of Geophysical Research: Earth Surface **126**(4), 2020–005657 (2021) https://doi.org/10.1029/2020JF005657

[43] MeteoSwiss: Hourly Precipitation Data from Automatic Weather Stations. Federal Office of Meteorology and Climatology, accessed October 2025. https://www.meteoswiss.admin.ch/services-and-publications/applications/ext/download-data-without-coding-skills.html#lang=en&mdt=normal&pgid=Precipitation&sid=BLA&col=ch.meteoschweiz.ogd-smn&di=daily&tr=recent&hdr=

[44] Zhou, G.G.D., Cui, K.F.E., Jing, L., Mangeney, A., Cui, Y., Huang, Y., Chen, X.: Segregation-induced flow transitions in rock-ice mixtures: Implications for rock-ice avalanche dynamics. Journal of Geophysical Research: Earth Surface **129**(9), 2024–007831 (2024) https://doi.org/10.1029/2024JF007831 https://agupubs.onlinelibrary.wiley.com/doi/pdf/10.1029/2024JF007831. e2024JF007831 2024JF007831

[45] Toney, L., Allstadt, K.E.: lsforce: A python-based single-force seismic inversion framework for massive landslides. Seismological Research Letters **92**(4), 2610–2626 (2021) https://doi.org/10.1785/0220210004 https://pubs.geoscienceworld.org/ssa/srl/article-pdf/92/4/2610/5350985/srl-2021004.1.pdf

[46] Allstadt, K.E., Toney, L., Collins, E.A.: lsforce (Version 1.1) [Source Code]. https://doi.org/10.5066/P9CR20KW . U.S. Geological Survey Software Release. https://doi.org/10.5066/P9CR20KW

[47] Kawakatsu, H.: Centroid single force inversion of seismic waves generated by landslides. Journal of Geophysical Research: Solid Earth **94**(B9), 12363–12374 (1989) https://doi.org/10.1029/JB094iB09p12363 https://agupubs.onlinelibrary.wiley.com/doi/pdf/10.1029/JB094iB09p12363

[48] Hibert, C., Stark, C.P., Ekström, G.: Dynamics of the oso-steelhead landslide from broadband seismic analysis. Natural Hazards and Earth System Sciences **15**(6), 1265–1273 (2015) https://doi.org/10.5194/nhess-15-1265-2015

[49] Hibert, C., Ekström, G., Stark, C.P.: The relationship between bulk-mass momentum and short-period seismic radiation in catastrophic landslides. Journal of Geophysical Research: Earth Surface **122**(5), 1201–1215 (2017) https://doi.org/10.1002/2016JF004027 https://agupubs.onlinelibrary.wiley.com/doi/pdf/10.1002/2016JF004027

[50] Gaume, J., Gast, T., Teran, J., Herwijnen, A., Jiang, C.: Dynamic anticrack propagation in snow. Nature Communications **9**(1), 3047 (2018) https://doi.org/10.1038/s41467-018-05181-w

[51] Blatny, L., Gray, J.M.N.T., Gaume, J.: A critical state μ(i)-rheology model for cohesive granular flows. Journal of Fluid Mechanics **997**, 67 (2024) https://doi.org/10.1017/jfm.2024.643

[52] Kreyszig, E.: Advanced Engineering Mathematics, 4th edn. Wiley, New York (1979)

[53] Jop, P., Forterre, Y., Pouliquen, O.: A constitutive law for dense granular flows. Nature **441**(7094), 727–730 (2006) https://doi.org/10.1038/nature04801

[54] Iverson, R.M., George, D.L.: A depth-averaged debris-flow model that includes the effects of evolving dilatancy. I. Physical basis. Proceedings of the Royal Society A: Mathematical, Physical and Engineering Sciences **470**(2170) (2014) https://doi.org/10.1098/rspa.2013.0819

[55] Iverson, R.M., George, D.L.: Modelling landslide liquefaction, mobility bifurcation and the dynamics of the 2014 Oso disaster. Geotechnique **66**(3), 175–187 (2016) https://doi.org/10.1680/jgeot.15.LM.004

[56] Bouchut, F., Fernández-Nieto, E.D., Mangeney, A., Narbona-Reina, G.: A two-phase two-layer model for fluidized granular flows with dilatancy effects. Journal of Fluid Mechanics **801**, 166–221 (2016) https://doi.org/10.1017/jfm.2016.417

[57] Munch, J., Zhuang, Y., Dash, R.K., Bartelt, P.: Dynamic thermomechanical modeling of rock-ice avalanches: Understanding flow transitions, water dynamics, and uncertainties. Journal of Geophysical Research: Earth Surface **129**(10), 2024–007805 (2024) https://doi.org/10.1029/2024JF007805

[58] Vicari, H., Tran, Q.-A., Metzsch Juel, M., Gaume, J.: The role of dilatancy and permeability of erodible wet bed sediments in affecting erosion and runout of a granular flow: Two-phase MPM–CFD simulations. Computers and Geotechnics **185**, 107307 (2025) https://doi.org/10.1016/j.compgeo.2025.107307

[59] Bouchut, F., Drach, E., Fernández-Nieto, E.D., Mangeney, A., Narbona-Reina, G.: A series of two-phase models for grain–fluid flows with dilatancy. Journal of Fluid Mechanics **1008**, 43 (2025) https://doi.org/10.1017/jfm.2025.131

[60] Schneider, D., Huggel, C., Haeberli, W., Kaitna, R.: Unraveling driving factors for large rock–ice avalanche mobility. Earth Surface Processes and Landforms **36**(14), 1948–1966 (2011) https://doi.org/10.1002/esp.2218 https://onlinelibrary.wiley.com/doi/pdf/10.1002/esp.2218

[61] Cappa, F., Guglielmi, Y., Viseur, S., Garambois, S.: Deep fluids can facilitate rupture of slow-moving giant landslides as a result of stress transfer and frictional weakening. Geophysical Research Letters **41**(1), 61–66 (2014) https://doi.org/10.1002/2013GL058566 https://agupubs.onlinelibrary.wiley.com/doi/pdf/10.1002/2013GL058566

[62] Yamada, M., Mangeney, A., Matsushi, Y., Matsuzawa, T.: Estimation of dynamic friction and movement history of large landslides. Landslides **15**(10), 1963–1974 (2018) https://doi.org/10.1007/s10346-018-1002-4

[63] Wang, C., Cui, Y., Song, D., Nie, J., Hu, B.: Effect of ice content on the interaction between rock–ice avalanche and rigid barrier: Physical and numerical modelling. Computers and Geotechnics **150**, 104924 (2022) https://doi.org/10.1016/j.compgeo.2022.104924

[64] Fan, X., Feng, Z., Ni, T., Deng, Y., Zhang, J., Dai, L.: The Friction Behavior of Rock-Ice Avalanches in Relation to Rock-Ice Segregation: Insights From Flume Physical Experiments. Journal of Geophysical Research: Earth Surface **130**(1), 2024–007904 (2025) https://doi.org/10.1029/2024JF007904

[65] Feng, Z., Fan, X., Ni, T., Deng, Y., Zou, C., Zhang, J., Xu, Q.: How Ice Particles Increase Mobility of Rock-Ice Avalanches: Insights From Chute Flows Simulation of Granular Rock-Ice Mixtures by Discrete Element Method. Journal of Geophysical Research: Earth Surface **128**(8), 2023–007115 (2023) https://doi.org/10.1029/2023JF007115

[66] Bowman, E.T., Take, W.A., Rait, K.L., Hann, C.: Physical models of rock avalanche spreading behaviour with dynamic fragmentation. Canadian Geotechnical Journal **49**(4), 460–476 (2012) https://doi.org/10.1139/t2012-007

[67] Jacquemart, M., Welty, E., Leopold, M., Loso, M., Lajoie, L., Tiampo, K.: Geomorphic and sedimentary signatures of catastrophic glacier detachments: A first assessment from flat creek, alaska. Geomorphology **414**, 108376 (2022) https://doi.org/10.1016/j.geomorph.2022.108376

[68] Iverson, R.M.: The physics of debris flows. Reviews of geophysics **35**(3), 245–296 (1997) https://doi.org/10.1029/97RG00426

[69] Coe, J.A., Bessette-Kirton, E.K., Geertsema, M.: Increasing rock-avalanche size and mobility in glacier bay national park and preserve, alaska detected from 1984 to 2016 landsat imagery. Landslides **15**(3), 393–407 (2018) https://doi.org/10.1007/s10346-017-0879-7

[70] Kristensen, L., Czekirda, J., Penna, I., Etzelmüller, B., Nicolet, P., Pullarello, J.S., Blikra, L.H., Skrede, I., Oldani, S., Abellan, A.: Movements, failure and climatic control of the veslemannen rockslide, western norway. Landslides **18**(6), 1963–1980 (2021) https://doi.org/10.1007/s10346-020-01609-x

[71] Jacquemart, M., et al.: Detecting the impact of climate change on alpine mass movements: a systematic review. Earth and Planetary Science Letters (2024). Online ahead of print at time of access

[72] Schneider, D., Bartelt, P., Caplan-Auerbach, J., Christen, M., Huggel, C., McArdell, B.W.: Insights into rock-ice avalanche dynamics by combined analysis of seismic recordings and a numerical avalanche model. Journal of Geophysical Research: Earth Surface **115**(F4) (2010) https://doi.org/10.1029/2010JF001734 https://agupubs.onlinelibrary.wiley.com/doi/pdf/10.1029/2010JF001734

[73] Grill, J., Strub, F., Altché, F., Tallec, C., Richemond, P.H., Buchatskaya, E., Doersch, C., Pires, B.Á., Guo, Z.D., Azar, M.G., Piot, B., Kavukcuoglu, K., Munos, R., Valko, M.: Bootstrap your own latent: A new approach to self-supervised learning. CoRR **abs/2006.07733** (2020) 2006.07733

[74] Vilajosana, I., Suriñach, E., Abellán, A., Khazaradze, G., Garcia, D., Llosa, J.: Rockfall induced seismic signals: case study in montserrat, catalonia. Natural Hazards and Earth System Sciences **8**(4), 805–812 (2008) https://doi.org/10.5194/nhess-8-805-2008

[75] Daly, R.A., Manger, G.E., Clark, J. Sydney P.: Section 4: Density of rocks. In: Handbook of Physical Constants. Geological Society of America, Boulder, CO (1966). https://doi.org/10.1130/MEM97-p19

[76] Cuffey, K.M., Paterson, W.S.B.: The Physics of Glaciers, 4th edn. Elsevier, Oxford, UK (2010)

[77] Bouchut, F., Mangeney-Castelnau, A., Perthame, B., Vilotte, J.-P.: A new model of Saint Venant and Savage–Hutter type for gravity driven shallow water flows. Comptes Rendus Mathematique **336**(6), 531–536 (2003) https://doi.org/10.1016/S1631-073X(03)00117-1

[78] Delannay, R., Valance, A., Mangeney, A., Roche, O., Richard, P.: Granular and particle-laden flows: from laboratory experiments to field observations. Journal of Physics D: Applied Physics **50**(5), 053001 (2017) https://doi.org/10.1088/1361-6463/50/5/053001

[79] Sulsky, D., Chen, Z., Schreyer, H.L.: A particle method for history-dependent materials. Computer Methods in Applied Mechanics and Engineering **118**(1-2), 179–196 (1994) https://doi.org/10.1016/0045-7825(94)90112-0 . Accessed 2023-02-06

[80] Drucker, D.C., Prager, W.: Soil mechanics and plastic analysis for limit design. Quarterly of Applied Mathematics **10**(2), 157–165 (1952) https://doi.org/10.1090/qam/48291

[81] Blatny, L., Gaume, J.: Matter (v1): An open-source mpm solver for granular matter. EGUsphere **2025**, 1–29 (2025) https://doi.org/10.5194/egusphere-2025-1157

[82] Vicari, H., Kyburz, M.L., Gaume, J.: Brief communication: Depth-averaging of 3D depth-resolved MPM simulation results of geophysical flows for GIS visualization. Natural Hazards and Earth System Sciences **25**(10), 3897–3904 (2025) https://doi.org/10.5194/nhess-25-3897-2025

[83] SN EN ISO 17892-4:2018-12: Geotechnische Erkundung Und Untersuchung, Laborversuch an Bodenproben – Teil 4: Bestimmung Der Korngrössenverteilung. Schweizerischer Verband der Strassen- und Verkehrsfachleute (VSS) (2018)

[84] ASTM D8550-25: Standard Test Method for Determination of Infiltration Rate and Calculating Field Hydraulic Conductivity of Field Soils by Sealed Single-Ring Infiltrometer and Multiple Pressure Head Procedure (2025)

[85] Vicari, H., Bründl, F., Frieß, P., Ringenbach, A., Stoffel, A., Bühler, Y., Aaron, J., McArdell, B., Walter, F., Graf, C., Herzog, R., Bebi, P., Gaume, J.: Linking debris flow erosion to channel-bed parameters: Geotechnical and remote sensing investigation of ten channels in Switzerland. ESS Open Archive (2025) https://doi.org/10.22541/essoar.176126762.20405430/v1

Frictional weakening in the highly mobile 2025 Blatten (Switzerland) rock–ice avalanche

Jiahui Kang[1,2*], Antoine Lucas[3], Anne Mangeney[3, 4], Johan Gaume[5,6], Kate Allstadt[7], Clément Hibert[8,9], Liam Toney[7], Hervé Vicari[5,6], Michael Dietze[9], Mylène Jacquemart[12,13], Marc Peruzzetto[11,3], Lars Blatny[6, 14], Michael L. Kyburz[5,6], Joachim Rimpot[8], Daniel Farinotti[12,13], Fabian Walter[1*]

[1*]Swiss Federal Institute for Forest, Snow and Landscape Research WSL, Birmensdorf, Switzerland.

[2*]Faculty of Geosciences and Environment, University of Lausanne, Lausanne, Switzerland.

[3]Institut de physique du globe de Paris, Université Paris Cité, CNRS, Paris, France.

[4]Institut Universitaire de France, Paris, France.

[5] WSL Institute for Snow and Avalanche Research SLF, Davos, Switzerland.

[6] Institute for Geotechnical Engineering, ETH Zürich, Zürich, Switzerland.

[7] U.S. Geological Survey, Geologic Hazards Science Center, Golden, Colorado, USA.

[8] Institut Terre et Environnement de Strasbourg (ITES), Université de Strasbourg, Strasbourg, France.

[9] Ecole et Observatoire des Sciences de la Terre (EOST), Université de Strasbourg, Strasbourg, France.

[10] Department of Geography, RWTH Aachen University, Aachen, Germany.

[11]BRGM, F-75012, Paris, France.

[12]Laboratory of Hydraulics, Hydrology and Glaciology (VAW), ETH Zürich, Zürich, Switzerland.

[13]Swiss Federal Institute for Forest, Snow and Landscape Research WSL, Sion, Switzerland.

[14]CNRS - UMR 7190, Institut Jean Le Rond d'Alembert, Sorbonne Université, Paris, France.

*Corresponding author(s). E-mail(s): jiahui.kang@wsl.ch; fabian.walter@wsl.ch;

Supplementary Information Overview

This Supplementary Information provides extended methodological details, parameter tests, and supporting results complementing the main text.

S1 describes the sensitivity analysis and quantitative performance metrics used to evaluate the numerical simulations against field and seismic observations.
S2 presents the detailed rheological parameter tests for the SHALlow water depth-averaged numerical model (SHALTOP) including the Coulomb, $\mu(\mathbf{u})$, Voellmy, and $\mu(I)$ rheologies.
S3 outlines the constitutive formulation and implementation of the Material Point Method model (MPM), emphasizing the Drucker–Prager framework and boundary conditions.

Supplementary **Table S1** summarizes the simulations for both the precursory event tests and best-fit parameters and evaluation metrics for each tested rheology of the main event.

Supplementary CSV file summarizes the complete set of simulation runs and the corresponding performance metrics used in the sensitivity analysis. Column *icomp* specifies the rheology type: 1 for pure Coulomb, 7 for $\mu(I)$, 8 for Voellmy, and 9 for $\mu(\mathbf{u})$.

Two Supplementary Videos accompany this material:
Video S1 illustrates the SHALTOP simulation results $\mu(I)$, showing the temporal evolution of flow thickness, friction angle and velocity with force history associated with seismic inversion.
Video S2 presents the full 3D animation of MPM $\mu(I)$ simulation.

S1. Sensitivity analysis and rheological parameter testing

Sensitivity analysis

Model-predicted forces were filtered and time-shifted to compare with the inverted force magnitude. Model–data fit was summarized by four metrics:

- **Trimline ratio [1]:** For each simulation, we first computed the dynamic simulated footprint as the area of the union of all grid cells exceeding a minimum flow thickness h_{th} of 0.05 m at any time step, and compared it against the area of the observed footprint (the entire mapped boundary polygon) mask using the intersection-over-union (IoU) formulation:

$$\text{TR} = \frac{|T_{\text{sim}} \cap T_{\text{obs}}|}{|T_{\text{sim}} \cup T_{\text{obs}}|}, \tag{1}$$

where T_{sim} and T_{obs} are the simulated and observed footprint areas, respectively.

- **Thickness Root-mean Squared Error:** The root-mean squared error (RMSE) between the observed and simulated final deposit thickness fields was calculated over all grid cells. The data is preprocessed by assigning $h = 0$ to no data cells in either thickness field, and to any cells in the observed deposits distribution with a negative thickness change or that is outside the observed footprint. This metric accounts for both vertical depth discrepancies and spatial mismatches:

$$\text{Thickness RMSE} = \sqrt{\frac{1}{N}\sum_{i=1}^{N}\left(h_i^{\text{sim}} - h_i^{\text{obs}}\right)^2}, \tag{2}$$

where h_i^{sim} and h_i^{obs} are the simulated and observed deposit thicknesses at grid i, respectively, and N is the number of grid cells.

- **Force normalized cross-correlation:** Median of the component-wise normalized cross-correlation between the modeled and inverted force histories, evaluated after aligning them by the optimal overall lag τ^*. τ^* is found by finding the time shift to identify the delay that maximizes the median normalized cross-correlation across all three components. The forward force-time histories were calculated with the acceleration of the landslide's center of mass at each time step, assuming a total volume of 9.35×10^6 m^3 and a bulk density of $2,113$ kg m^{-3}. For each component $k \in \{E, N, U\}$, we computed the normalized cross-correlation using the "*correlate_template*" function from ObsPy [2]. The correlation was evaluated over the common analysis window T and maximized over allowed time lags. The overall metric is the median across the three components.
  This measure yields the maximum correlation coefficient (with a value of 1 indicating perfect correlation, 0 indicating no correlation) of the two force histories, normalized by their energy, and is independent of amplitude.

- **Force amplitude root-mean squared error:** RMSE of the modeled versus inverted absolute force amplitudes after aligning the inverted force history to the modeled by shifting the inverted signal by the optimal overall lag τ^*, averaged over the three components, expressed as follows:

$$\text{Amp RMSE} = \sqrt{\frac{1}{3T}\sum_{k\in\{E,N,U\}}\sum_{t=1}^{T}\left(F_k^{\text{sim}}(t) - F_k^{\text{inv}}(t-\tau^*)\right)^2}. \tag{3}$$

We compute the force amplitude RMSE only over the time window between 40 and 120 seconds relative to the zero time of the model simulations to focus on best matching the peak portion of the signal.

The full list of simulations and corresponding performance metrics is provided in Supplementary Table 1. Simulations in which the flow propagated beyond the mapped topographic domain were flagged as invalid and excluded from the best-fit evaluation. To enable a consistent comparison across metrics with different units and scales, we normalized each metric by computing its z -score relative to the ensemble mean and standard deviation. Because lower RMSE values indicate better performance, the z-scores of the Thickness RMSE and Amplitude RMSE metrics were sign-inverted before aggregation. To derive the overall performance index, we computed a weighted sum of the normalized scores across all four metrics. As detailed in the main text, topographic deposit metrics were assigned a weight of 0.7, whereas seismic metrics were weighted at 0.3.

S2. Main event rheological parameter testing for SHALTOP

For every rheology, parameter tests were performed over physically reasonable intervals derived from laboratory and field constraints. The Coulomb rheology assumes a constant basal friction coefficient $\mu = \tan\delta$. We tested δ between 6° and 9° in 1° increments to determine the minimum angle reproducing the observed runout. Friction angle of 8° yielded the best overall match but tended to under-represent lateral spreading. The volume-dependent $\mu(V)$ law is given by $\mu(V) = V^{-0.0774}$ [3].

To account for dynamic weakening, we tested a velocity-weakening law, derived from this series of simulation, where the friction coefficient is no longer constant as opposed to the Coulomb friction law, but varies with the flow velocity [3]:

$$\mu(\mathbf{u}) = \begin{cases} \mu_{\mathbf{u}1} + \frac{\mu_{\mathbf{u}2} - \mu_{\mathbf{u}1}}{||\mathbf{u}||/u_w}, \text{ if } \quad ||\mathbf{u}|| > u_w \\ \mu_{\mathbf{u}2} \quad \text{otherwise,} \end{cases} \tag{4}$$

where $\|\mathbf{u}\|$ is the norm of the flow velocity and u_w is a characteristic transition velocity defining the onset of dynamic weakening. We explored lower friction angles $\delta_{\mathbf{u}1}$ between 6° and 8° (in 1° increments), whereas keeping the upper friction angle fixed as $\delta_{\mathbf{u}2} = \delta_{\mathbf{u}1} + 10°$ for consistency with empirical calibration tests. The characteristic velocity u_w was set to 2 m/s.

For the Voellmy rheology, the basal shear stress is expressed as [4]

$$\frac{T}{\rho} = \cos\theta g h \mu \left(1 + \frac{\mathbf{u}^\top \mathcal{H} \mathbf{u}}{g \cos\theta}\right) + g\frac{||\mathbf{u}||^2}{\xi}, \tag{5}$$

where ρ is the bulk density, h is the flow thickness in the direction perpendicular to the topography, θ is the slope angle, and $\mathcal{H}$ the curvature tensor. We tested friction angles δ of 5° and 6°, and for each case varied ξ between 2000, 2500, and 3000 m s^{-2}.

The combination $\delta = 5°$ and $\xi = 2500$ m/s^2 yielded the highest overall performance based on the composite z-score. However, as this score represents an unweighted sum across all metrics, the result should be interpreted as indicative rather than optimal. In particular, the corresponding deposit remains less laterally extensive than in the $\mu(I)$ simulations.

Lastly, for $\mu(I)$ rheology [5], it accounts for strain rate-dependent friction:

$$\mu(I) = \mu_{I1} + \frac{\mu_{I2} - \mu_{I1}}{1 + I_0/I}, \tag{6}$$

where the inertial number I can be expressed in depth-averaged models as:

$$I = \frac{5}{2} \frac{d||\mathbf{u}||}{h\sqrt{\varphi g h \cos(\theta)}}, \tag{7}$$

where μ_{I1} and μ_{I2} are the lower and upper limits of the friction coefficient, respectively, $I_0 = 0.279$ is an empirical coefficient calibrated on lab experiments of granular flows, d is of the order of the mean grain size, and φ is the solid fraction The dimensionless number I represents the ratio between the microscopic timescale for particle rearrangement and the macroscopic timescale for deformation [6]. We first varied δ_1 between 1° and 5° in 1° increments, keeping the upper friction angle fixed as $\delta_{I2} = \delta_{I1} + 10°$. For each friction pair, the characteristic grain size d was varied among 0.1, 0.3, 0.5, and 0.7 m. However, noticing that this fixed 10° difference did not fully account for the geometry of the final deposition stage, we also varied the space between δ_{I1} and δ_{I2} to fully explore the parameter space. The best-fitting configuration ($\delta_{I1} = 1°$, $\delta_{I2} = 16°$, $d = 0.3$ m, $\varphi = 0.4$) achieved one of the highest composite scores and reproduced the most laterally extensive deposit geometry, consistent with enhanced flow mobility (see detailed sensitivity test in the CSV file).

S3. Constitutive details of 3D MPM granular flow modeling

For the sake of simplicity, calibration, and comparison with the SHALTOP-$\mu(I)$ framework, we opted for a cohesionless and rate-dependent Drucker–Prager model. The stress states are bounded by the yield condition $y(p, q) \leq 0$, where the yield function is defined as:

$$y(p, q) = q - \mu^{\text{int}}(I)p, \tag{8}$$

Here, the yield surface is expressed in terms of the stress invariants

$$p = -\tfrac{1}{3}\text{tr}(\boldsymbol{\sigma}) \quad \text{and} \quad q = \sqrt{\tfrac{1}{2}\boldsymbol{\sigma}_d : \boldsymbol{\sigma}_d}\,, \tag{9}$$

where $\boldsymbol{\sigma}$ is the Kirchhoff stress tensor and $\boldsymbol{\sigma}_d$ its deviatoric part.

The internal friction coefficient $\mu^{\text{int}}(I)$ is rate-dependent and analogously to Equation (6),

$$\mu^{\text{int}}(I) = \mu_1^{\text{int}} + \frac{\mu_2^{\text{int}} - \mu_1^{\text{int}}}{1 + I_0/I}, \tag{10}$$

is the internal friction which depends on the inertial number $I = \frac{\dot{\gamma}\, d}{\sqrt{p\varphi/\rho}}$ where $\dot{\gamma}$ denotes the plastic shear strain rate.

A non-associative flow rule is assumed, with the plastic potential function equal to q. As in [7], the isotropic and hyperelastic Hencky model is used to relate stresses to elastic deformations (Young's modulus $E = 1$ MPa and Poisson's ratio $\nu = 0.3$). The elastoplastic problem is solved within the general finite strain framework of [8].

The explicit MPM solver used in this study features a regular and uniform grid with cell width 4 m and maximum duration of 250 s, relying on B-spline interpolation functions for points-grid interpolation and an Affine Fluid-Implicit-Particle transfer scheme [9]. We therefore have an uncertainty in particle position, and consequently in deposit height, on the order of $dx/2 = 2$ m. To ensure consistency in the comparison, the topography in the MPM simulations was smoothed using an 8 m spatial window, matching the 8 m grid resolution used in SHALTOP.

For the basal boundary condition, we apply a slip criterion that allows positive slope-normal velocities. Introducing a base friction μ, the velocity $\boldsymbol{v}$ at the boundary is given by

$$\boldsymbol{v} = \begin{cases} \boldsymbol{v}_T^* - \mu\, ||\boldsymbol{v}_N^*|| \dfrac{\boldsymbol{v}_T^*}{||\boldsymbol{v}_T^*||} & \text{if } ||\boldsymbol{v}_T^*|| > \mu\, ||\boldsymbol{v}_N^*||, \\ \boldsymbol{0} & \text{otherwise,} \end{cases} \tag{11}$$

where $\boldsymbol{v}_T^*$ and $\boldsymbol{v}_N^*$ are the tangential and normal components, respectively, of the velocity $\boldsymbol{v}^*$ *before* (marked by *) the boundary condition is applied. To allow separation from the boundary, this is only applied if $\boldsymbol{v}^*$ indicates penetration of the boundary; otherwise $\boldsymbol{v} = \boldsymbol{v}^*$. Such a boundary condition is extensively used in MPM flow modeling and has been rigorously validated [7, 10].

Finally, again following the $\mu(I)$ rheology and Equation (6), we impose the base friction to be $\mu = \mu(I_{\text{col}})$, where I_{col} is the inertial number of the (local) material colliding with the boundary. As such, the base friction is bound by two parameters, μ_1 and μ_2. To best reproduce the run-out distance, deposit height and seismic force, we used the following combination of parameters: $\delta_1^{\text{int}} = \tan^{-1}(\mu_1^{\text{int}}) = 2°$, $\delta_2^{\text{int}} = \tan^{-1}(\mu_2^{\text{int}}) = 40°$, $\mu_1 = 0.02$, $\mu_2 = 0.28$, $d = 0.3$ m, $\varphi = 0.7$, $I_0 = 0.01$.

In the so-called pure Coulomb case, we assume that the basal friction μ and internal friction μ^{int} are constant and equal. To best fit the run-out distance with this model, we used $\mu = \mu^{\text{int}} = 0.21$.

Table S1 Summary of numerical simulation parameters and performance metrics for the precursory sequence and the main event.

Scenario	**Model**	**Rheology laws**	**Volume**(m^3)	**Friction parameters**	**Weighted z-score**
Precursory sequency (Fam. 1)	SHALTOP	Coulomb	$500 - 300,000$	$\delta = 10°$	–
	SHALTOP	Coulomb	$500 - 300,000$	$\delta = 20°$	–
	SHALTOP	Coulomb	$500 - 300,000$	$\delta = 30°$	–
	SHALTOP	$\mu(V)$	$500 - 300,000$	–	–
Precursory sequency (Fam. 2)	SHALTOP	Coulomb	$500 - 30,000$	$\delta = 10°$	–
	SHALTOP	Coulomb	$500 - 30,000$	$\delta = 20°$	–
	SHALTOP	Coulomb	$500 - 30,000$	$\delta = 30°$	–
	SHALTOP	$\mu(V)$	$500 - 30,000$	–	–
Main event	SHALTOP	Coulomb	9.35×10^6	$\delta = 8°$	-0.09
	SHALTOP	$\mu(I)$	9.35×10^6	$\delta_1 = 2°$, $\delta_2 = 16°$, $I_0 = 0.279$, $d = 0.3$ m, $\varphi = 0.7$	1.36
	SHALTOP	$\mu(\mathbf{u})$	9.35×10^6	$\delta_1 = 17°$, $\delta_2 = 7°$, $u_w = 2$ m/s	0.66
	SHALTOP	Voellmy	9.35×10^6	$\delta_1 = 5°$, $\xi = 2500$ m s^{-2}	1.27
	SHALTOP	$\mu(V)$	9.35×10^6	–	-6.27
	MPM	Coulomb	9.35×10^6	$\delta = 11.8°$	-0.45
	MPM	$\mu(I)$	9.35×10^6	$\delta_1 = 1°$, $\delta_2 = 16°$, $I_0 = 0.01$, $d = 0.3$ m, $\varphi = 0.7$	1.05

References

[1] Galas, S., Dalbey, K., Kumar, D., Patra, A., Sheridan, M.: Benchmarking TITAN2D mass flow model against a sand flow experiment and the 1903 frank slide. In: Ho, K., Li, V. (eds.) Proceedings of the 2007 International Forum on Landslide Disaster Management, pp. 899–918. Geotechnical Division, The Hong Kong Institution of Engineers, Hong Kong (2007). Hong Kong, 10–12 December

2007

[2] Beyreuther, M., Barsch, R., Krischer, L., Megies, T., Behr, Y., Wassermann, J.: Obspy: A python toolbox for seismology. Seismological Research Letters **81**(3), 530–533 (2010) https://doi.org/10.1785/gssrl.81.3.530 https://pubs.geoscienceworld.org/ssa/srl/article-pdf/81/3/530/2762059/530.pdf

[3] Lucas, A., Mangeney, A., Ampuero, J.P.: Frictional velocity-weakening in landslides on earth and on other planetary bodies. Nature Communications **5**(1), 3417 (2014) https://doi.org/10.1038/ncomms4417

[4] Rocha, F.M., Johnson, C.G., Gray, J.M.N.T.: Self-channelisation and levee formation in monodisperse granular flows. Journal of Fluid Mechanics **876**, 591–641 (2019) https://doi.org/10.1017/jfm.2019.518

[5] Jop, P., Forterre, Y., Pouliquen, O.: A constitutive law for dense granular flows. Nature **441**(7094), 727–730 (2006) https://doi.org/10.1038/nature04801

[6] Pouliquen, O., Forterre, Y.: Friction law for dense granular flows: Application to the motion of a mass down a rough inclined plane. Journal of Fluid Mechanics **453** (2002) https://doi.org/10.1017/S0022112001006796

[7] Blatny, L., Gray, J.M.N.T., Gaume, J.: A critical state μ(i)-rheology model for cohesive granular flows. Journal of Fluid Mechanics **997**, 67 (2024) https://doi.org/10.1017/jfm.2024.643

[8] Simo, J.C.: Algorithms for static and dynamic multiplicative plasticity that preserve the classical return mapping schemes of the infinitesimal theory. Computer Methods in Applied Mechanics and Engineering **99**(1), 61–112 (1992) https://doi.org/10.1016/0045-7825(92)90123-2

[9] Fei, Y., Guo, Q., Wu, R., Huang, L., Gao, M.: Revisiting integration in the material point method: A scheme for easier separation and less dissipation. ACM Transactions on Graphics **40**(4), 1–16 (2021) https://doi.org/10.1145/3450626.3459678

[10] Blatny, L., Gaume, J.: Matter (v1): An open-source mpm solver for granular matter. EGUsphere **2025**, 1–29 (2025) https://doi.org/10.5194/egusphere-2025-1157